UHASSELT
KNOWLEDGE IN ACTION

Maastricht University

Faculty of Medicine and Life Sciences
School for Life Sciences
Master of Biomedical Sciences

Master's thesis

Exploring Schwann cell dysfunction in CMT1A using human-derived 2D/3D mono- and co-culture systems

Stephanie Van de Vyver

Thesis presented in fulfillment of the requirements for the degree of Master of Biomedical Sciences, specialization Molecular Mechanisms in Health and Disease

SUPERVISOR :

Prof. dr. Esther WOLFS

MENTOR :

Mevrouw Nathalie DIRKX

2024
2025

Transnational University Limburg is a unique collaboration of two universities in two countries: the University of Hasselt and Maastricht University.

UHASSELT
KNOWLEDGE IN ACTION

www.uhasselt.be
Universiteit Hasselt
Campus Hasselt:
Martelarenlaan 42 | 3500 Hasselt
Campus Diepenbeek:
Agoralaan Gebouw D | 3590 Diepenbeek

UHASSELT
KNOWLEDGE IN ACTION

Maastricht University

Faculty of Medicine and Life Sciences
School for Life Sciences
Master of Biomedical Sciences

Master's thesis

Exploring Schwann cell dysfunction in CMT1A using human-derived 2D/3D mono- and co-culture systems

Stephanie Van de Vyver

Thesis presented in fulfillment of the requirements for the degree of Master of Biomedical Sciences, specialization Molecular Mechanisms in Health and Disease

SUPERVISOR :

Prof. dr. Esther WOLFS

MENTOR :

Mevrouw Nathalie DIRKX

Exploring Schwann Cell Dysfunction in Charcot-Marie-Tooth Disease Type 1A Using Human-Derived 2D/3D Mono- and Co-Cultures*

Van de Vyver S.[1,2], Dirkx N.[2], Lambrechts I.[2], Van Den Bosch L.[3], and Wolfs E.[2]

[1]Hasselt University, Faculty of Medicine and Life Sciences, Campus Diepenbeek, Agoralaan Building D – B-3590 Diepenbeek
[2]Hasselt University, Department of Cardio and Organ Systems, Functional Imaging & Research on Stem cells (FIERCE) lab, Biomedical Research Institute, Agoralaan Building C – B-3590 Diepenbeek
[3]VIB-KULeuven, Center for Brain & Disease Research, Herestraat 49 – B-3001 Leuven

*Running title: *Exploring Schwann cell dysfunction in CMT1A*

To whom correspondence should be addressed: Prof. dr. Esther Wolfs, Tel: +32 (11) 26 92 96; Email: esther.wolfs@uhasselt.be

Keywords: Charcot-Marie-Tooth disease type 1A, peripheral myelin protein 22, Schwann cell dysfunction, human dental pulp stem cells (DPSC), co-cultures

ABSTRACT

Charcot-Marie-Tooth disease type 1 (CMT1A) is the most prevalent inherited demyelinating peripheral neuropathy, caused by a duplication of the peripheral myelin protein 22 (PMP22) gene. This results in Schwann cell (SC) dysfunction and aberrant peripheral nerve myelination, ultimately leading to progressive motor and sensory deficits. To overcome the limited translational relevance of traditional CMT1A models, we applied our pioneering method using dental pulp stem cells (DPSCs) from four CMT1A patients and control donors. These cells were differentiated into SC-like cells (DPSC-SCs) and used to investigate disease-related SC phenotypes, validate differentiation status, and explore neuron-SC-extracellular matrix interactions in CMT1A. This study revealed marked inter-donor heterogeneity in SC-related gene expressions, including myelin-related, transcriptional, and adhesion/ECM-associated genes, collectively suggesting that SCs adopt an immature, repair-like phenotype in CMT1A. Additionally, neurotrophic factor secretion (BDNF, GDNF, βNGF, NT3), assessed by enzyme-linked immunosorbent assay, showed donor-specific alterations in SC-neuron communication. Furthermore, 2D and 3D co-culture systems with induced pluripotent stem cell-derived motor neurons (iPSC-MNs) and CMT1A DPSC-SCs exhibited impaired migration toward neurons. In 3D collagen I hydrogels, CMT1A DPSC-SCs demonstrated reduced interaction with surrounding collagen compared to the control. Conclusively, our findings validated a promising patient-derived *in vitro* model, through which heterogeneous aberrant SC phenotypes were elucidated. Moreover, the model proposes that these CMT1A SCs adopt a persistent repair-like state, mimicking injury responses and contributing to disease pathology.

INTRODUCTION

Charcot-Marie-Tooth (CMT), also termed as hereditary motor and sensory neuropathy (HMSN), was first described in 1886 by physicians Jean-Marie Charcot, Pierre Marie, and Howard Henry Tooth, and later named in their honor (1). CMT is the most common inherited peripheral neuropathy worldwide, affecting approximately 1 in 2500 individuals of all ages and ethnicities (1-3). The disease comprises a genetically heterogeneous collection of hereditary disorders that primarily affect myelinating Schwann cells (SCs) and peripheral axons. Consequently, this causes chronic motor and sensory peripheral polyneuropathy, which typically manifests in the distal limbs with muscle weakness and atrophy, sensory loss, foot deformities like *pes cavus*, areflexia, and other symptoms . However, the disease severity varies between subtypes, some of which are associated with more severe phenotypes (5). This heterogeneous spectrum of subtypes is defined by electrophysiological, age-related, genetic, and inheritance-based criteria. Traditionally, classification was based on nerve conduction velocities, distinguishing three main types: primary demyelinating (CMT1; <15-35 m/sec), primary axonal (CMT2; >45 m/s), and intermediate (30-45 m/sec) forms (2-4, 6). Further classification of the three main groups is

based on genetic etiology, with over 100 genes harboring pathogenic variants that have been identified as causative or contributory to CMT pathogenesis. These genes are involved in diverse molecular pathomechanisms and contribute to significant phenotypic heterogeneity (1, 3, 7, 8). Most of the subtypes are associated with either a mutation or copy number variation in a single key causative gene: *Peripheral Myelin Protein 2 (PMP22), Myelin Protein Zero (MPZ), Gap Junction Protein Beta-1 (GJB1),* or *Mitofusin 2 (MFN2)*, collectively accounting for 80-90% of genetic diagnosed CMT cases (1, 3, 6). The remaining cases involve a range of other genes or remain genetically unresolved (9, 10). Moreover, inheritance patterns also vary and include autosomal dominant, autosomal recessive, X-linked, and, more rarely, sporadic forms (1-3). Together, the diversity in genetic causes, inheritance modes, and clinical presentation underscores the marked heterogeneity of CMT (2, 11).

CMT type 1A (CMT1A) is the most prevalent demyelinating form, accounting for 50-70% of all diagnosed CMT cases (2). This condition results from a 1.5-megabase tandem duplication on chromosome 17p11.2, caused by unequal crossover between misaligned CMT1A-REP elements during meiosis, which leads to overexpression of *PMP22* (12-14). This gene is predominantly expressed in SCs, the glial cells of the peripheral nervous system (PNS) responsible for myelination. During development, SCs form myelin sheaths by spirally wrapping their lipid-rich membranes around large peripheral axons, enabling accelerated nerve conduction and providing axonal protection (11, 15). *PMP22* expression in SCs is driven by cell-specific promoter P1, whereas the alternative promoter P2 is weakly active in non-neuronal tissue (6, 13, 14, 16, 17). Consequently, myelinating SCs produce high levels of the exon 1A transcript, which encodes the hydrophobic transmembrane glycoprotein PMP22 (2, 6, 8, 13, 14, 17). This protein accounts for 2-5% of total myelin proteins in the compact regions of myelin sheaths that surround all myelinated fibers in the PNS (2, 8, 13). Although its biological function is not yet fully understood, researchers suggest that PMP22 may play a role in myelin stability and myelination processes . Additionally, PMP22 is also proposed to play a vital role in SC proliferation, differentiation, and maturation at the pre-myelinating stage (6, 11, 18). Thus, *PMP22* overexpression induces SC dysfunction and subsequently impairs (re)myelination, which are core hallmarks of CMT1A (19).

In the PNS, neurons rely on SCs for myelination to enhance signal transduction and structural support, while axon-derived cues such as neuregulin-1 (NRG1) regulate SC proliferation, differentiation, phenotypic specialization, myelination, and extracellular matrix (ECM) synthesis (20-22). In turn, SCs secrete neurotrophic factors, such as Brain-Derived Neurotrophic Factor (BDNF), Glial Cell Line-derived Neurotrophic Factor (GDNF), Neurotrophin 3 (NT3), and Beta Nerve Growth Factor (βNGF) (23-26). These promote neuronal survival, axonal (out)growth, and regeneration, thereby establishing a supportive regenerative niche for nerve repair (21, 23, 24, 26, 27).
In parallel, SCs actively construct and remodel the ECM by synthesizing structural components such as collagens, fibronectin, and laminins that form the basal lamina surrounding both SCs and axons (21, 23, 25, 27, 28). Hence, this SC-specific ECM provides a biochemical scaffold that supports migration, SC alignment, and stable axonal interactions (21, 25). Moreover, the ECM interacts with SC surface receptors, such as integrins, to modulate intracellular signaling pathways that control their proliferation, survival, differentiation, and migration. (21, 28, 29). Additionally, these interactions also play a crucial role in regulating myelination. Specifically, the interaction between the SC receptor β1 integrin with ECM components, primarily laminin, supports axon sorting, basal lamina assembly, and the differentiation of SCs into a myelinating phenotype (30, 31). Beyond SC dysfunction, dysregulated extrinsic signaling and disrupted interactions within the peripheral nerve microenvironment are believed to contribute to the pathogenesis of CMT1A. In particular, dynamic interactions between SCs, neurons, and the ECM are thought to play a critical role in modulating CMT1A disease progression (32-34).

To date, no effective treatment currently exists for CMT1A beyond symptom-alleviating supportive care, which leaves patients with a poor quality of life (35-38). Hence, researchers have investigated various therapeutic strategies targeting different aspects of CMT1A, but no breakthrough has yet been achieved (7, 8, 36, 38, 39). For instance, ascorbic acid was among the first therapies tested, initially showing promise by reducing *PMP22*

expression in a CMT1A mouse model. However, despite offering valuable mechanistic disease insights, it ultimately failed to meet primary endpoints in clinical trials (8, 38). Similarly, PXT3003, a polytherapy designed to downregulate *PMP22* overexpression and the most advanced candidate for market approval in CMT1A, showed promising results in rodent studies but faced issues with drug crystallization, subsequent patient dropout, and stability at high concentrations (8, 36, 38). Beyond pharmacological approaches, gene-mediated strategies have also been explored, targeting *PMP22* using, among others, antisense oligonucleotides, short hairpin RNA, CRISPR/Cas, small interfering RNA, as well as viral vector-based approaches. Although these have shown preclinical promise, they have so far failed to demonstrate clinical success in humans (7, 8, 36, 38, 39). These ongoing challenges reflect the persistent drawback of transitioning seemingly effective preclinical candidate treatments into successfully clinically FDA-approved therapies, with many failing during the translation phase (7, 8, 35, 36, 38, 39). This major obstacle in CMT1A therapy development lies in the limited translational relevance of traditional CMT1A models (8, 35).

Traditionally, CMT1A pathophysiology studies have relied using rodent *in vivo* models. The first animal models with *PMP22* and myelin abnormalities were Trembler (J) mice. They carry missense mutations in *PMP22* but lack the characteristic copy number variation seen in CMT1A patients. Hence, to better recapitulate CMT1A, transgenic models with *PMP22* overexpression were developed. These include mice carrying additional murine *PMP22* copies, such as TgN248 (16 copies), My41 (unspecified extra copies), and Jp18 (one or two extra copies); as well as transgenic models expressing human *PMP22,* like C22 (seven copies), C61 (four copies), and C3 (three to four copies). While these models align more closely with the human CMT1A genotype and phenotype than Trembler models, reliability issues persist (6, 40, 41). Firstly, due to cloning technique limitations, none of the existing animal models can capture the large 1.5 Mb DNA duplication characteristics of CMT1A (6, 35). Hence, these models were created by random insertion of multiple human PMP22 cDNAs and therefore fail to fully reflect their human genetic complexity (35). Secondly, excessive *PMP22* copies in models like C22 and C61 fail to adequately replicate the gene duplication characteristics as seen in the human disease (6). Thirdly, species-specific differences, such as the 22-amino acid divergence between human and mouse *PMP22* protein, further challenge their translational relevance (40).

Although existing *in vivo* models have advanced our understanding of the genetic, biological, and molecular basis of CMT1A pathogenesis, their limitations contribute to the high failure rate of preclinical therapies in clinical trials (35). However, the use of primary human SCs is not a viable alternative due to both ethical and practical constraints. Their isolation requires invasive nerve biopsies, which pose risks of neurological impairment or healthy tissue damage, and offer restricted access to viable tissue. Moreover, these procedures lead to prolonged recovery and yield few viable cells due to low proliferation capacity (42-47). Additionally, postmortem SC isolation is equally challenging, as SCs rapidly degrade after death (48). This highlights the urgent need for a more translationally relevant alternative that accurately reflects human disease pathology. Therefore, induced pluripotent stem cells (iPSCs) were created by reprogramming an individual's isolated somatic cells using Yamanaka factors. Subsequently, these cells can differentiate into any cell type from the three germ layers, under defined culture conditions with appropriate transcription factors to mimic developmental signaling cues *in vitro* (49-51). Consequently, iPSCs derived from patients preserve the human origin and the patient's genetic signature *(*50*,* 51*)*. This enables accurate reproduction of human CMT1A phenotypes with improved reliability and clinical relevance (52-54). Nevertheless, despite their proven utility in modeling various neurological disorders, iPSCs also present limitations, including complex and invasive extraction procedures, lengthy differentiation protocols, risk of uncontrolled proliferation, potential tumorigenicity, and variability in differentiation (25, 35, 54-56). To overcome these challenges, we propose human dental pulp stem cells (DPSCs) as a promising alternative in CMT1A research. DPSCs are mesenchymal stem cells found in the dental pulp of human teeth. Hence, DPSCs can be easily and non-invasively obtained from extracted third molars, which are commonly considered medical waste, thereby avoiding ethical concerns and procedural complexities (57, 58). Moreover, DPSCs possess a high proliferative potential, self-renewal

abilities, clonogenicity, and they retain their stem cell properties after cryopreservation (57, 59-62). Since DPSCs are neural-crest-derived stem cells, they are already lineage-committed and naturally predisposed to differentiate into nerve and glial cells, including SCs (20, 58). Therefore, Martens et al. have pioneered a validated method to successfully differentiate DPSCs into functional, myelinating SCs *(57, 58)*. In contrast with iPSCs, the DPSC differentiation does not require prior reprogramming procedures, which makes the process more efficient, less time-consuming, and reduces the risk of uncontrolled proliferation or tumorigenesis. Importantly, by pioneering the biobanking of DPSCs from healthy donors and CMT1A patients, we preserved the donor's specific genetic background (58). As a result, DPSC-derived SCs (DPSC-SCs) represent an innovative and clinically relevant human model for studying SC biology and accurately recapitulating CMT1A-specific phenotypes and morphologies as observed in patients (51, 57, 63).

In this study, we will generate four CMT1A and normal control DPSC lines, followed by differentiation into corresponding DPSC-SC lines. This approach is crucial, as CMT1A presents with highly heterogeneous phenotypes across patients, which we aim to include in this study (64, 65). Subsequently, mono-cultures of DPSCs or DPSC-SCs, as well as 2D/3D co-cultures containing healthy iPSC-derived motor neurons (iPSC-MNs) with either control or CMT1A DPSC-SCs will be created. With these models, we aim to explore multiple aspects of CMT1A-related Schwann cell biology dysfunctions. Firstly, this study will characterize the phenotypes of DPSCs and DPSC-SCs , and assess the heterogeneity of SC biology across four patient lines compared to controls. Secondly, the influence of aberrant *PMP22* expression on SC differentiation in CMT1A will be investigated to identify potential targets for improving differentiation. Thirdly, the communication of SCs on neurons will be assessed by examining the release of neurotrophic factors and exploring disrupted SC-axon interaction in CMT1A. Lastly, we will explore the interactions between the ECM, SCs, and neurons in CMT1A.

EXPERIMENTAL PROCEDURES

DPSC collection – CMT1A patient-derived and control third molars were voluntarily donated during dental extractions (Table S1). All. donors or their legal guardians provided written informed consent. Sample collection and use were approved by the medical ethics committee of Ziekenhuis Oost-Limburg (ZOL, Genk, Belgium). Subsequent DPSC isolation was conducted according to the explant method as described before (58, 66).

DPSC differentiation into DPSC-SCs – At 80-95% confluency, DPSCs were subcultured and differentiated into DPSC-SCs using the validated methodology extensively described by Martens et al. and Libberecht et al. (57, 58). Briefly, to initiate differentiation, DPSCs were seeded on Poly-L-Lysine (PLL; Sigma Aldrich; 1/30)-coated flasks and cultured for 24h in serum-deprived standard medium supplemented with 1 mM β-mercaptoethanol (BME; Gibco) (Table S2). Medium was then replaced with DPSC medium containing 35 ng/mL trans-retinoic acid (tRA) for 72h (Table S2). Thereafter, cells were cultured in DPSC medium supplemented with 1 ng/mL neuregulin 1 (NRG1; ImmunoTools), 0.5 ng/mL forskolin (ImmunoTools), 0.1 ng/mL fibroblast growth factor 2 (FGF2; ImmunoTools), and 0.1 ng/mL platelet-derived growth factor (PDGF; ImmunoTools) (Table S2). Cells were maintained in this final differentiation medium for two weeks, with medium changes every 2-3 days.

Cell culture of DPSC and DPSC-SC – DPSCs and DPSC-SCs were cultured on PLL-coated flasks in their respective media (Table S2). At 80-95% confluency, cells were washed with PBS, dissociated with 0.05% Trypsin-ethylenediaminetetraacetic acid (Trypsin-EDTA; Sigma) for 5 min at 37°C, neutralized with media, and centrifuged at 300 x g for 5 min prior to passaging.

iPSC-MN differentiation – The healthy iPSC line SCC271 (Sigma-Aldrich) was cultured on Matrigel™ (Corning) coated 6-well plates in Essential™ 8 medium (Gibco), supplemented with 1000 U/mL penicillin/streptomycin (P/S; Sigma) (Table S2). To preserve their undifferentiated state, iPSCs were kept at 40-50% confluency, with manual colony picking and medium changes every other day. Subsequently, iPSCs were differentiated into iPSC-MNs following the validated methodology established by the lab of Ludo Van Den Bosch (67).

2D and 3D co-cultures – For both 24-well plate and microfluidic co-culture systems, coverslips were coated with Poly-L-Ornithine (PLO; Sigma Aldric; 1/30) for 3h at 37°C followed by laminin (L2020-1MG; Sigma) coating overnight at 37°C. On Day 10 (D10) of

Van Den Bosch's iPSC-MN differentiation methodology, cells were seeded either directly on the coated coverslips for the 24-well plate co-cultures (7,200k cells/well) or into the upper two wells of a RD150 (XONA™ microfluidics) device placed on a coated coverslip (125k cells/well) (67). One week later, DPSC-SCs were added in a 4:1 ratio to the iPSC-MNs, either onto the 24-well plate coverslips (10.8k cells/well) or onto the remaining two lower wells of the XONA™ device (60k cells/cm³).

For 3D hydrogel co-cultures, DPSC-SCs (250k cells/mL gel) and D10 iPSC-MN (250k cells/mL gel) were combined into a single cell suspension. 10% of this suspension was mixed with 10% Minimum Essential Medium (MEM; Merck) and 80% type I tail collagen (5 mg/mL in 0.6% acetic acid, First Link), and neutralized with 10 mM sodium hydroxide. Next, 1 mL of this mixture was transferred at 4°C into a preformed mold with tethering mesh at opposite ends and polymerized at 37°C for 10 min. Gels were then immersed in co-culture medium (Table S2).

Maintenance of cells – Cells and co-cultures were maintained in their respective media (Table S2), with medium changes performed 2-3 times a week, and preserved at 37°C in a humidified 5% CO_2 incubator.

Western Blot – Proteins were harvested from DPSC and DPSC-SCs (30k cells/3.5 cm²) using in-house made radioimmunoprecipitation assay (RIPA) buffer supplemented with protease and phosphatase inhibitors (Roche). After 20 min at 4°C, cells were scraped, centrifuged at 13,000 x g for 10 min at 4°C, and then supernatant was stored at -80°C. Protein concentration was measured and quantified using the Pierce™ BCA Protein Assay Kit (ThermoFisher), according to the manufacturer's instructions, at 570 nm (Bio-Rad plate reader). Next, 10 µg/mL protein lysate samples were diluted 1:1 with reducing sample buffer supplemented with 5% BME and denatured for 5 min at 95°C. Subsequently, the standard ladder (Bio-Rad) and samples were loaded into 12% SDS-PAGE gels. Electrophoresis was then performed in a running buffer at an increasing gradient between 100 to 150 V, for a maximum of 120 min (PowerPac Basic, Bio-Rad). Proteins were then transferred from the gel to a 0.2 µm PVDF membrane in transfer buffer at 350 mA for 1 h (PowerPac HC, Bio-Rad). After blocking the membranes for 1 h in 5% Marvel PBS at room temperature (RT), the membranes were incubated with the primary antibody PMP22 (OriGene; 1:150 in 5% Marvel PBS) overnight at 4°C while shaking. After washing three times with 0.05% Tween-20 PBS, the secondary antibody polyclonal rabbit anti-mouse immunoglobulins/HRP (Dako; 1/1000 in 5% Marvel PBS) was added 1 h in the dark while shaking at RT. After washing, protein bands were visualized with SuperSignal™ West Atto Ultimate Sensitivity Substrate (Thermo Scientific) and imaged with the chemiluminescent Amersham™ Imager 680 (Thermo Fisher). For normalization, blots were stripped with a mild buffer for 1 h before re-probing with the reference protein GAPDH (Santa Cruz Biotechnology; 1/1000 in 5% Marvel PBS)**.** PMP22 band intensity was quantified and normalized to GAPDH using ImageJ.

RNA isolation and cDNA synthesis – Cells were seeded on PLL-coated culture flasks (100k/T25) to 90% confluency. Then, cells were lysed in QIAzol (Qiagen), and stored at -80°C. Total RNA was extracted using the NZY Total RNA Isolation Kit (NZYtech) according to the manufacturer's instructions. Afterwards, RNA purity, quality, and concentration were assessed with a NanoDrop Spectrophotometer. cDNA synthesis was performed using Qscript (Quanta-bio), and amplified on a T100 Thermal Cycler (BioRad) with the following cycle: 5 min at 25°C, 30 min at 42°C, 5 min at 85°C, and hold at 4°C. The solution was then diluted to 3 ng/µL with Milli-Q water (MQ) and stored at -20°C.

Quantitative PCR – In a 96-well plate, 7.5 µL of master mix consisting of MQ, a primer pair (Table S3), and SYBR Green (Thermo Fisher Scientific), was added to 2.5 µL cDNA sample or MQ (blank). After plate centrifugation, the qPCR-reaction was started on a QuantStudio 3 **(**Thermo Fisher Scientific) using the following cycling conditions: 95°C for 20 sec (hold stage); 95°C for 3 sec and 60°C for 30 sec (PCR stage; repeated for 40 cycles); 60°C for 1 min and 95°C for 15 sec (melt curve stage). Relative gene expression was quantified using the 2-ΔΔCq normalized to the validated housekeeping gene *PGK1*

Immunocytochemical or confocal microscopy and image analysis – For 2D cultures, cells were seeded on PLL-coated glass coverslips (15k cells/cm³) in their appropriate culture medium (Table S2). Mono- and co-cultures were fixed in 4% paraformaldehyde (PFA) for 20 min at 4°C. After washing with PBS, cells were permeabilized with 0.05% Triton-X100 in PBS for 30 min at 4°C. Subsequently, after washing, cells were blocked

with 10% protein blocking buffer (Dako) for 20 min at RT, followed by overnight incubation with primary antibodies (Table S4; diluted in blocking buffer) at 4°C while shaking. The next day, after washing, secondary antibodies (Table S4; 1/500 dilution in blocking buffer) were applied for 2 h in the dark at RT. After washing, the nuclei were counterstained with Hoechst (Table S4; 1/150 dilution in blocking buffer) for 30 min in the dark. Finally, after washing, cells were mounted with Immunomount (Thermo Scientific). ICC images were acquired with a Leica DM400 B LED fluorescence microscope. Confocal images were acquired with LSM880 (Zeiss), employing the Maitai (810 nm) function for the second harmonic generation (SHG) imaging of hydrogels. ImageJ was used to quantify fluorescence intensity using the formula: $\frac{area*mean}{amount\ of\ cells,}$, integrated density, and migration distance.

Enzyme-linked immunosorbent assay – DPSCs and DPSC-SCs were cultured on PLL-coated culture flasks (140k cells/T75). 24 h after seeding, DPSC and DPSC-SCs' medium was changed to culture medium with adapted 2% heat-inactivated Fetal Calf Serum (hiFCS) (Table S2). After 48 h, conditioned medium was collected on ice, and centrifuged at 300 RPC at 4°C. Next, the supernatant was filtered using 33 mm syringe filters and transferred to Vivaspin® tubes on ice for concentration by centrifugation at 8,000 x g for ±3-5h at 4°C. BDNF, GDNF, βNGF, and NT3 secretion was assessed using the Human ELISA Kits (RayBiotech) according to the manufacturer's instructions. Protein concentrations were used for normalization.

Statistical analysis **–** Data were statistically analyzed using GraphPad Prism v9 (GraphPad Software Inc.) and reported as mean ± SEM. For all datasets, outliers were removed using the Rout test, and normality was assessed with the Shapiro-Wilk test before analysis. Subsequently, for normally distributed data, a one-way student t-test or ANOVA followed by Tukey's post hocmultiple comparison test was used. For non-normally distributed data, a one-way Mann-Whitney U test or Kruskal-Wallis test followed by a Dunn's multiple comparison test was applied. Statistical significance between groups was considered as *P < 0.05, **P < 0.01, ***P < 0.001, ****P < 0,0001.

RESULTS

DPSCs show successful differentiation into SC phenotypes – DPSCs derived from four CMT1A patients and control donors were differentiated into SC-like cells (DPSC-SCs). Morphological changes were observed by brightfield microscopy at key time points (D0, 1, 4, 11, and 18), showing a consistent transition toward a mature SC phenotype in both groups. At pre-differentiation (D0), DPSCs exhibited a fibroblast-like morphology with flattened, oval to round, spindle-shaped cell bodies and minimal processes. By D1, after BME induction, slight elongation and short process formation emerged. On D4, following tRA addition, cells appeared larger with more prominent, rounded somas, indicative of increased cytoplasmic volume. By D11, following sustained exposure to growth factor, cells demonstrated a well-defined bipolar morphology, characterized by elongated cell bodies and defined processes extending from both ends of the soma. This coincided with the onset of cellular orientation and partial alignment. At the final stage, D18, cells had acquired a mature SC-like morphology, characterized by thin, elongated bipolar cell bodies and pronounced, extended processes emerging from either side of the soma, forming interwoven, parallel networks. Conclusively, these observations suggest successful morphological differentiation of DPSCs into DPSC-SCs in both groups (Fig. 1A).

To confirm a successful differentiation, ICC was performed for established SC markers, including S100 Calcium-Binding Protein B (S100β), P75 Neurotrophic Receptor ($P75^{NTR}$), Jun Proto-Oncogene AP-1 Transcription Factor Subunit (CJUN), PMP22, and Laminin (LAM) in a control cell line (Fig. 1B-F). Quantification revealed a significant increase in S100β (1.6-fold; P=0.0003) and CJUN (1.4-fold; P=0.0289) protein levels in DPSC-SCs compared to undifferentiated DPSCs, indicating successful acquisition of SC identity. Contrary, $P75^{NTR}$ levels remained stable, while PMP22 and LAM showed a slight, non-significant decrease following differentiation (Fig. 1G-K).

Confirmation of successful DPSC-SC differentiation in CMT1A while preserving pathological signatures – To evaluate whether the presence of CMT1A pathology affects the

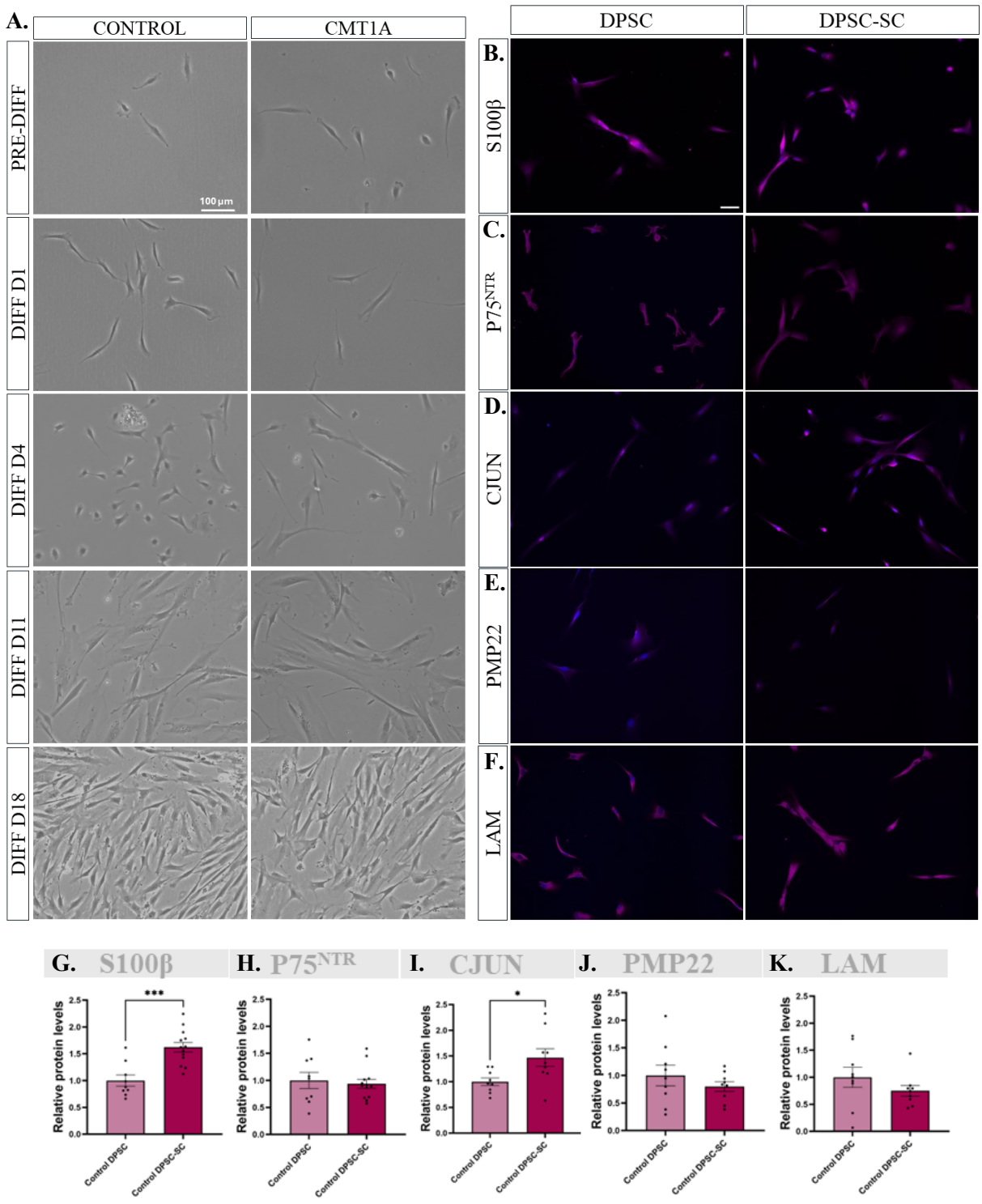

Fig. 1 – Fig. 1 – ***Healthy and CMT1A-derived DPSC-SCs exhibit SC phenotypes.*** (**A**) Representative brightfield images showing the morphological transition of healthy and CMT1A-derived DPSCs into DPSC-SCs at key differentiation time points (D0, 1, 4, 5, 11, and 18). Initially compact and fibroblast-like DPSCs progressively elongate and develop bipolar processes, culminating in a mature, elongated, spindle-shaped, bipolar SC morphology by D18. No morphological differences were observed between control and CMT1A lines. Scale bar: 100 µm. **(B-F)** Representative immunofluorescent images of established SC markers (magenta) stained for **(B)** S100β, **(C)** $P75^{NTR}$, **(D)** CJUN, **(E)** PMP22, **(F)** LAM. Nuclei are counterstained with Hoechst (Blue). Scale bar; 100 µm. **(G-K)** Quantification of relative protein levels of **(G)** S100β, **(H)** P75, **(I)** CJUN, **(J)** PMP22, **(K)** LAM. Data is analyzed by fold change of integrated density, normalized against the mean of control DPSCs. Data is presented as the mean ± SEM (N=3 coverslips/condition). *P < 0.05, ***P < 0.001; one-way Mann-Whitney U test (G-K). *Abbreviations are listed in Table S5.*

efficiency of DPSC differentiation into DPSC-SCs, relative LAM protein levels were compared pre- and post-differentiation in both control and CMT1A cell lines, and across conditions (Fig. 2A). In both conditions, LAM levels significantly increased following differentiation ($P<0.0001$), with similar 5.6-fold and 5.0-fold elevations in control and CMT1A cells, respectively. Notably, relative LAM levels were highly comparable between control and CMT1A DPSCs as well as between their differentiated DPSC-SCs, indicating that both conditions underwent a consistently effective differentiation process (Fig. 2B).

Having established that differentiation efficiency is unaffected, the persistence of molecular CMT1A features in the DPSC-SC model was subsequently evaluated. Therefore, *PMP22* mRNA expression and protein levels were analyzed in four CMT1A and control DPSC and DPSC-SCs. qPCR analysis demonstrated that all CMT1A donors exhibited a reduction in *PMP22* mRNA expression upon differentiation,

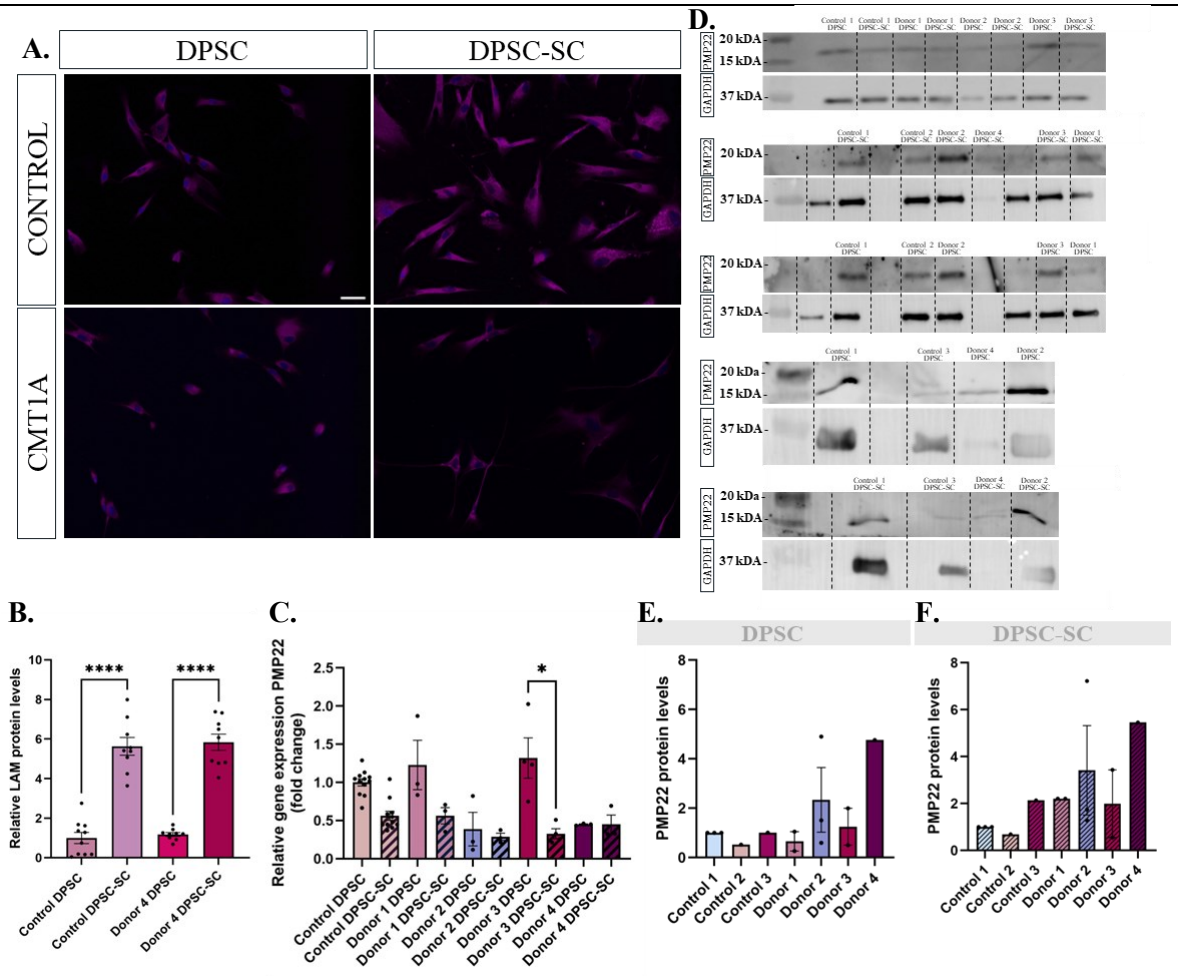

Fig. 2 – **Successful CMT1A DPSC-to-DPSC-SC differentiation while preserving pathological characteristics.** Representative immunofluorescent images of established SC marker LAM (magenta) in control and CMT1A lines before- and after differentiation. Nuclei are counterstained with Hoechst (Blue). Scale bar; 100 µm. **(B)** Quantification of relative LAM protein level. Data is analyzed by fold change of integrated density, normalized against the mean of control DPSCs. Data is presented as the mean ± SEM (N=3 coverslips/condition). **(C)** *PMP22* mRNA expression levels in four CMT1A-derived as well as a pool of control DPSC and DPSC-SCs. Data is presented as mean ± SEM, normalized toward the reference gene *PGK1* and the mean of control DPSCs ($N\geq3$). **(D)** Western blot of PMP22 protein bands (17 kDa) of 4 CMT1A-derived and 3 control DPSCs and DPSCs (N=1-3). **(E-F)** Western blot quantification of PMP22 protein (17 kDA) levels among three controls and four CMT1A-donors at **(E)** DPSC stage or **(F)** DPSC-SC stage. Data is analyzed as the relative protein, normalized by the reference protein GADPH 36 (kDa) and the mean of control 1 DPSC. Data is presented as mean ± SEM (N=1-3). $^{*}P < 0.05$, $^{***}P < 0.001$; ANOVA followed by Tukey's post hocmultiple comparison test (B) and one-way Kruskal-Wallis with Dunn's multiple comparison (C). *Abbreviations are listed in Table S5.*

consistent with the control group, although the extent of downregulation varied across donors. Exceptionally, donor 3 showed a significant 4.0-fold decrease (P=0.0250) post-differentiation. Remarkably, *PMP22* mRNA levels in all CMT1A DPSC-SCs were lower than, or comparable to, those observed in control DPSC-SCs (Fig. 2C).

Additionally, Western Blot analysis was performed on DPSC and DPSC-SC lysates from these four CMT1A donors and three healthy controls (Fig. 2D). At the DPSC stage, PMP22 protein levels were comparable in control 1 and 3, whereas control 2 exhibiting 1.9-fold reduction relative to the other controls. Among CMT1A lines, donor 1 showed moderate, 1.5-fold decreased PMP22 levels compared to control 1 and 3, while remaining 1.3-fold higher than control 2. Conversely, donor 3 displayed a mild increase, whereas both donor 2 and 3 demonstrated markedly elevated levels of PMP22 compared to all controls (Fig. 2E). Following differentiation, control lines 1 and 2 exhibited similar PMP22 protein levels, whereas control 3 showed a modest increase, 2.1- and 3.1-fold higher than control 1 and 2, respectively. Notably, all CMT1A DPSC-SCs presented elevated PMP22 levels compared to all controls (Fig. 2F). Collectively, these findings confirm that DPSCs can successfully differentiate into DPSC-SCs in a CMT1A context, with disease-associated characteristics remaining preserved post-differentiation.

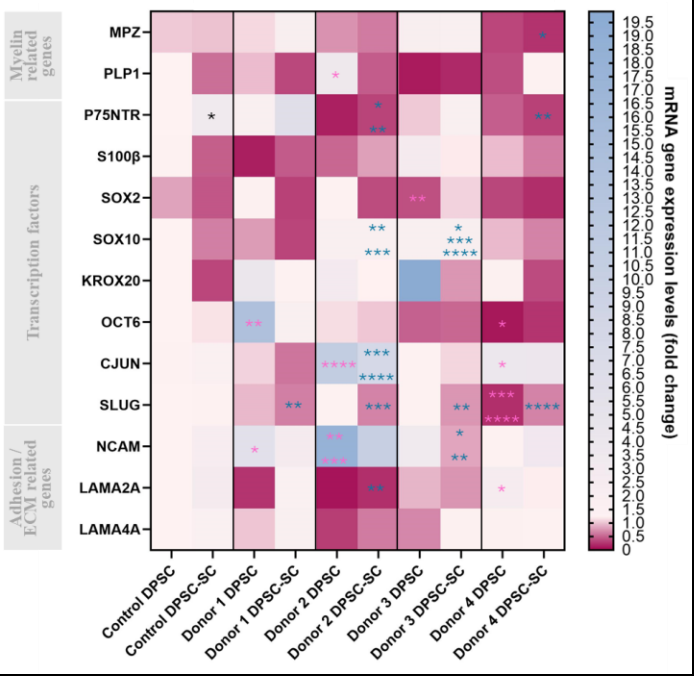

Fig. 3 – ***CMT1A reveals inter-donor heterogeneity in SC-relevant genes.*** Heatmap of the mRNA expression levels of 13 SC-related genes in four CMT1A-derived as well as a pool of control DPSC and DPSC-SCs. Data is presented as mean ± SEM, normalized toward the reference gene *PGK1* and the mean of control DPSCs per gene (N≥3). Black asterix: significant changes between DPSCs and DPSC-SCs from the same donor. Purple asterix: significant changes between DPSCs across different donors. Blue asterix: significant changes between DPSC-SCs across different donors. *P < 0.05, **P< 0.01 ***P < 0.001, ****P < 0,0001. *Abbreviations are listed in Table S5.*

CMT1A reveals inter-donor heterogeneity in SC-relevant genes – To unravel SC phenotypic variation in CMT1A, qPCR was conducted on 13 SC-relevant genes, including myelin-associated, SC transcriptional identity, and ECM/adhesion-related genes. mRNA gene expression was assessed before and after the differentiation of DPSCs from four donors and a pool of controls into corresponding DPSC-SCs. Firstly, myelin-related genes *MPZ* and *Proteolipid Protein 1* (*PLP1*) expression levels were examined. *MPZ* showed variable expression patterns across CMT1A donors. While expression remained stable upon differentiation in the control group, donors 2 and 4 exhibited minimal reduction, whereas donor 1 showed a marked 2.2-fold increase, and donor 3 a pronounced 1.19-fold decrease. Additionally, *MPZ* expression levels in donor 4 DPSC-SCs were significantly lower compared to donors 1 (P=0.0423; 10.2-fold) and 3 DPSC-SCs (P=0.0390; 8.8-fold), highlighting substantial inter-donor variability in both *MPZ* expression levels and response to differentiation. *PLP1* expression also diverged; donors 1 and 2 confirmed the expected control-like decrease, while donors 3 and 4 demonstrated an increase post-differentiation. Notably, *PLP1* expression in donor 2 DPSCs was higher than in other donor DPSCs, with a significant difference compared to donor 3 DPSCs (P=0.0132; 38.7-fold) (Fig. 3, S6).

Secondly, expression levels of key SC transcription factors were evaluated. For $P75^{NTR}$, differentiation induced an upregulation in all groups, consistent with the significant 3.4-fold increase observed in the control group (P=0.0443), except for donor 4. Donor 4 showed a decrease upon differentiation, significantly reduced compared to donor 1 (P=0.0099; 23.4-fold) and the control (P=0.0063; 12.9-fold)

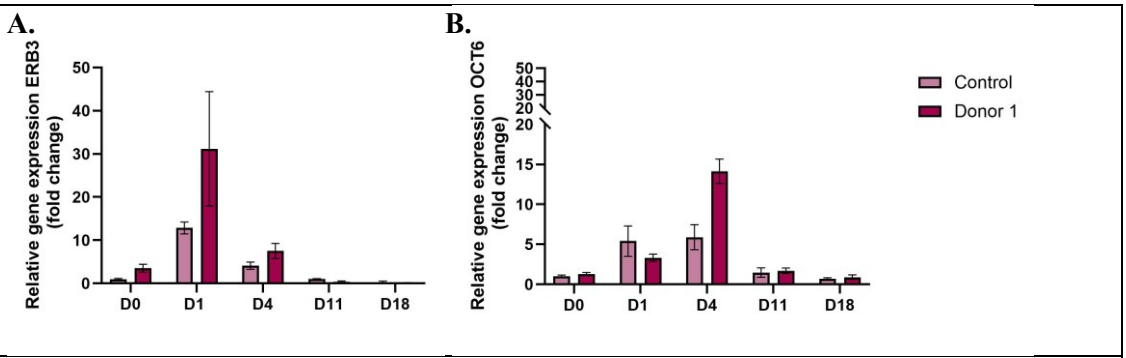

Fig. 4 – **Preserved temporal expression patterns of *ERB3* and *OCT6* in CMT1A and control conditions during differentiation. (A-B)** mRNA expression levels of **(A)** *ERB3* and **(B)** *OCT6* in CMT1A-derived as well as control DPSC and DPSC-SCs at different key points of the differentiation (D1, D4, D11, D18). Data is presented as mean ± SEM, normalized toward the reference gene *PGK1* and the mean of control DPSCs (N=3). One-way Kruskal-Wallis with Dunn's multiple comparison. *Abbreviations are listed in Table S5.*

DPSC-SCs. Furthermore, *P75^{NTR}* expression levels were inter-donor variable, with donor 2 DPSC-SC showing significantly lower expression compared to both control (P=0.0073; 12.6-fold) and donor 1 (P=0.0110; 22.9-fold) DPSC-SCs (Fig. 3; Fig. S6). *S100β* mRNA expression decreased post-differentiation in control, donor 3, and donor 4, while donors 1 and 2 showed an increase from initially lower expression levels in their DPSCs. More specifically, *S100β* expression was significantly lower in donor 1 DPSCs compared to donor 3 DPSCs (P=0.0085; 25,3-fold). *SRY-Box Transcription Factor 2 (SOX2)* expression decreased in all conditions following differentiation, except for donor 3, which showed an upregulation. Following differentiation, *SRY-Box Transcription Factor 10 (SOX10)* mRNA levels decreased in control, donor 1, and donor 4, but slightly increased in donors 2 and 3, which also displayed generally higher expression levels in their DPSCs relative to those of the other groups. Therefore, donor 3 DPSC-SCs expressed significantly more *SOX10* than control (P=0.0008; 3.9-fold), donor 1 (P<0.0001; 7.5-fold), and donor 4 (P=0.0126; 3.8-fold) DPSC-SCs. Donor 2 DPSC-SCs expressed significantly more *SOX10* than control (P=0.0070; 3.6-fold) and donor 1 (P=0.0007; 6.8-fold). Both *Early Growth Response Protein 2 (KROX20)* and *POU Class 3 Homeobox 1 (OCT6)* mRNA expression consistently declined post-differentiation across all donors, although donor 4 had significantly lower *OCT6* expression at the DPSC stage compared to control (P=0.0207; 12.5-fold) and PxC3 (P=0.0011; 175.81-fold) DPSCs. In contrast, *CJUN* expression increased in the control group, but decreased in all CMT1A donors upon differentiation. Notably, donor 2 and donor 4 showed generally higher *CJUN* expression levels compared to the other conditions. Donor 2 demonstrated significantly *CJUN* expression in both DPSC and SC stages compared to all the other conditions, while the expression in donor 4 DPSCs was also significantly elevated relative to the control DPSCs (P=0.0446; 4.0-fold). *Snail Family Transcriptional Repressor 1 (SLUG)* expression increased after differentiation in the control and donor 4, whereas it decreased in the other CMT1A donors. Specifically, all CMT1A donor DPSC-SCs showed significantly lower *SLUG* expression compared to control DPSC-SCs. Additionally, donor 4 DPSCs exhibited significantly lower *SLUG* levels compared to control (P<0.0001; 5.5-fold), donor 2 (P=0.0001; 5.6-fold), and donor 3 (P<0.0001; 6.2-fold) DPSCs, while donor 4 DPSC-SCs showed significant lower expression compared to control DPSC-SCs (P<0.0001;) (Fig. 3; Fig. S6).

Lastly, adhesion and ECM-related gene expression were examined. *Neural Cell Adhesion Molecule (NCAM)* expression increased in control and donor 4, but decreased in all other donors after differentiation. Thereby, donor 1 (P=0.0134, 5.6-fold) and donor 2 (P=0.0002; 18.0-fold) DPSCs exhibited significantly higher *NCAM* levels than the control. Moreover, donor 2 DPSCs demonstrated significantly higher *NCAM* expression compared to those in donor 4 DPSCs (P=0.0052), while donor 3 DPSC-SCs had significantly lower expression compared to donors 2 (P=0.00037) and 4 (P=0.0426) DPSC-SCs. *Laminin Subunit Alpha 2 (LAMA2A)* expression increased after differentiation in the control, donor 1, and 2, whereas it decreased in

donors 3 and 4 . Notably, donor 4 DPSCs expressed significantly higher *LAMA2A* levels than donors 1 (P=0.0352) and 2 (P=0.0134), while donor 2 DPSC-SCs exhibited significantly reduced (P=0.0019) expression than control DPSC-SCs. In contrast, *Laminin Subunit Alpha 4 (LAMA4A)* expression increased post-differentiation in all donors, except donor 4, which showed a slight 1.2-fold reduction (Fig. 3; Fig. S6). Altogether, this approach revealed markedly inter-donor heterogeneity among CMT1A donors, underscoring the phenotypic complexity of the disease.

CMT1A cells show conserved expression dynamics of ERBB3 and OCT6 during SC differentiation - To investigate potential disruptions in phenotypic SC differentiation associated with CMT1A, the expression dynamics of two-stage-specific SC genes at key differentiation time points (D1, D4, D11, and D18). Expression analysis of *Receptor Tyrosine-Protein Kinase ERBB3 (ERB3)* showed a similar temporal expression pattern between control and CMT1A donor cells. However, expression levels were consistently slightly elevated in the CMT1A condition across all time points. At D0, corresponding to the DPSC stage, *ERRB3* expression was low but detectable in both conditions. Upon initiation of differentiation (D1), a marked upregulation of *ERB3* expression was observed, showing a 12.8-fold and a more pronounced *31.2*-fold increase in control and CMT1A cells, respectively. This was followed by a downregulation trend over subsequent time points. At D4, *ERB3* expression decreased by 3.2-fold in donor and 4.1-fold in CMT1A cells. On D11, decline continued with a 4.1-fold and 18.3-fold decrease in control and donor cells, respectively. Eventually, by D18, *ERB3* levels had further decreased by 3.2-fold in controls and 2.8-fold in CMT1A donors (Fig. 4A)

Similar observations were made for *OCT6*. At D0, *OCT6* expression levels were comparable between control and CMT1A-derived cells. Upon initiation of differentiation (D1), *OCT6* expression increased moderately, showing a 5.4-fold upregulation in control cells and a 2.6-fold increase in CMT1A cells, resulting in slightly diverging expression levels between the two conditions. At D4, expression levels remained unchanged between control cells (1.0-fold), while a notable 4.3-fold increase was observed in CMT1A-derived cells. Following this peak, expression levels gradually declined in both conditions. By D11, *OCT*6 expression showed a 4.0-fold decrease in control cells and a 14.1-fold decrease in CMT1A cells, leading to similar expression levels between both groups at this stage. Finally, at D18, *OCT6* expression further decreased, with a 2.1-fold downregulation in controls and a 0.9-fold reduction in *CMT1A* cells, again converging to comparable levels across conditions (Fig. 4B).

In conclusion, *ERBB3* and *OCT6* show comparable trends during SC differentiation in both control and CMT1A cells, indicating preserved differentiation dynamics. However, differences in expression levels at certain time points suggest subtle dysregulation that may contribute to CMT1A-related dysfunction.

CMT1A donors exhibit altered neuron-SC interactions in 2D co-cultures - Given the role of SCs in supporting neuronal growth and survival through the secretion of neurotrophic factors, levels of four key neurotrophic factors: BDNF, GDNF, NT-3, and βNGF were measured in conditioned medium using ELISA. Secretion levels were compared within each cell line before and after differentiation as well as between CMT1A and healthy control lines, to assess both differentiation-induced and disease-related changes.

BDNF secretion showed an increasing trend following differentiation in nearly all lines, including control 2 and 3, as well as donor 1 and 3. Specifically, donor 1 showed a significant 37.47-fold change elevation (P=0.0303) post-differentiation. Contrarily, BDNF levels slightly decreased in control 1 after differentiation, whereas donor 3 showed a more pronounced reduction. Overall, all DPSC lines exhibited comparable levels of BDNF secretion, with the exception of control 1 and donor 4, which showed elevated BDNF levels. In contrast, considerable variation in BDNF concentrations was observed among the different DPSC-SC groups. Notably, BDNF levels secreted by donor 3 DPSC-SCs were significantly lower than those of control 3 (P=0.0402; 29.17-fold) and donor 1 (P=0.0107; 70.98-fold) DPSC-SCs (Fig. 5A). For NT-3 secretion, a consistent decreasing trend was observed across all cell lines following differentiation, with the exception of control 3, which displayed an opposing trend with increased levels. NT3 concentrations were comparable among control 2, donor 1, and donor 3 DPSCs, all of which secreted higher levels than the other DPSCs, which exhibited uniformly lower levels.

Conversely, NT3 levels were largely similar among DPSC-SCs, with the exception of control 1 and donor 4, which showed lower concentrations (Fig. 5B). For βNGF secretion, levels remained relatively stable in control 1 and donor 3 after differentiation, whereas donor 4 showed a decrease. Initially, βNGF concentrations varied among the DPSC lines,

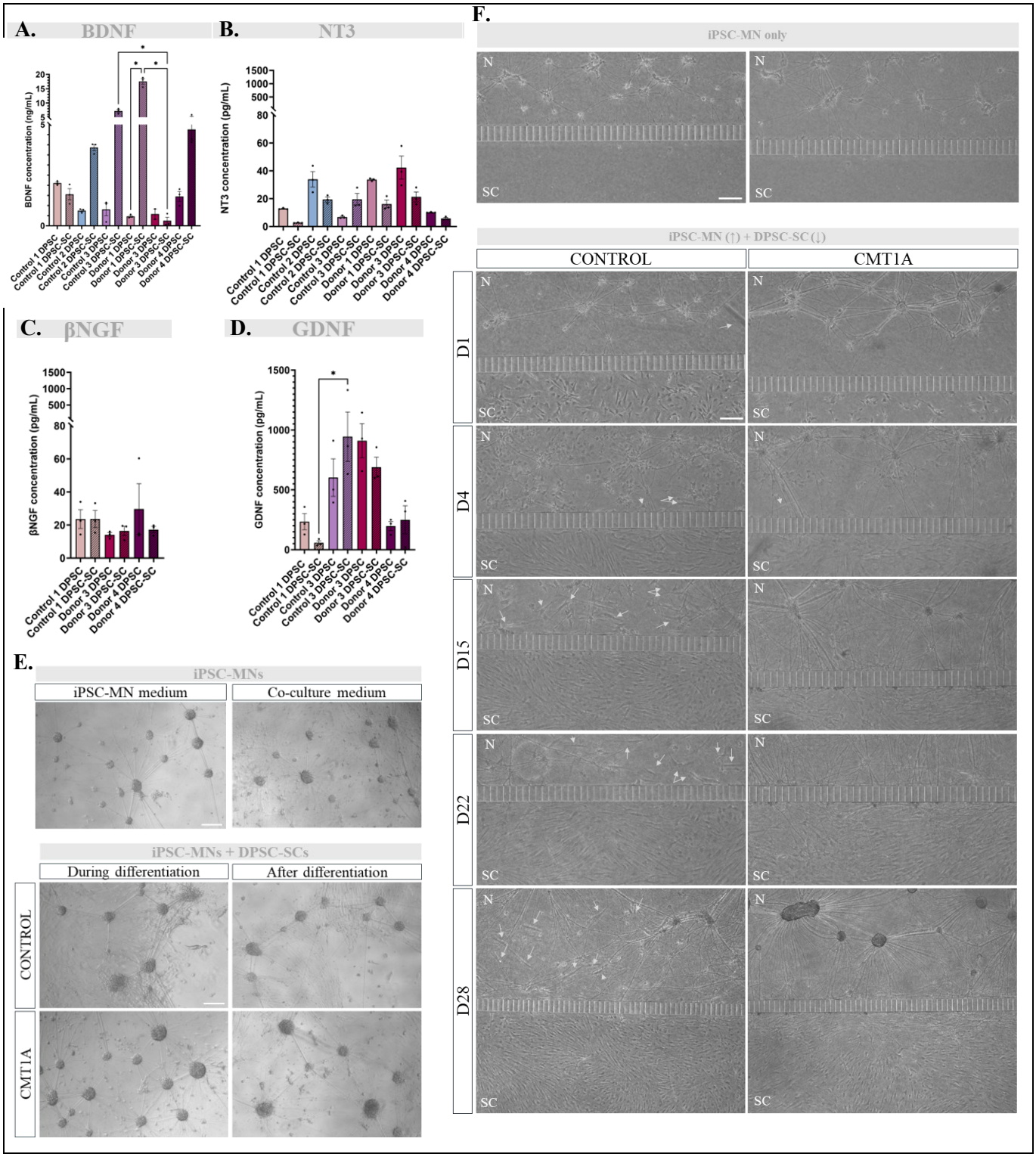

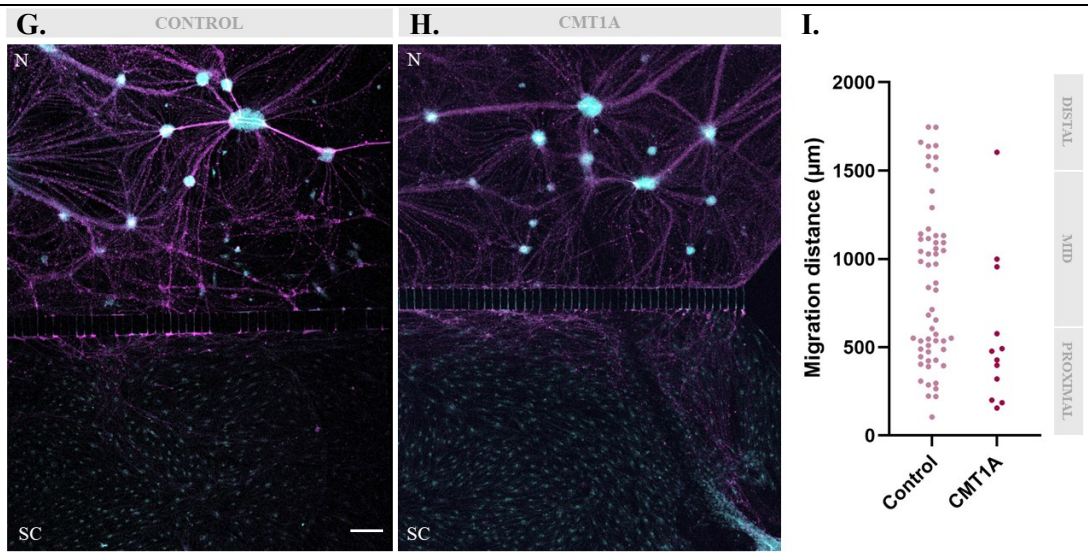

Fig. 5 – ***CMT1A donors exhibit altered neuron-SC interactions in 2D co-cultures.*** **(A-D)** Quantification of neurotrophic secretion for **(A)** BDNF, **(B)** NT3, **(C)** βNGF, **(D)** GDNF measured across normal control as well as CMT1A-derived DPSCs and DPSC-SCs (N=3). **(E)** Representative brightfield images showing neuron-SC interactions in a 24-well plate co-culture containing iPSC-MN and either differentiating or fully differentiated DPSC-SCs under four conditions. Condition 1: iPSC-MNs in iPSC-MN medium. Condition 2: iPSC-MNs in co-culture medium. Condition 3: iPSC-MNs with control DPSC-SCs in co-culture medium. Condition 4: iPSC-MNs with CMT1A DPSC-SCs in co-culture medium. Scale bar; 200 µm. **(F)** Representative brightfield images of a microfluidic device containing differencing iPSC-MNs with either normal control or CMT1A-derived DPSC-SCs. Arrows: Differences in SC migration capacity and axonal projections were observed across healthy and CMT1A conditions over time (D1, 4, 15, 22). N; neuronal compartment; SC; Schwann cell compartment; Arrows; migrated DPSC-SCs; Scale bar; 200 µm. **(G-H)** Corresponding confocal microscopy images at D28 stained for S100β (cyan; DPSC-SCs) and BIIItub (magenta; iPSC-MNs) in **(G)** control or **(H)** CMT1A conditions. N; neuronal compartment; SC; Schwann cell compartment; Scale bar; 200 µm. **(I)** Corresponding quantification of migration capacity by DPSCs. Data are presented as a scatter plot, indicating their migration distance (N=1). *P < 0.05; one-way Kruskal-Wallis and Dunn's multiple comparison test. *Abbreviations are listed in Table S5.*

with donor 3 showing reduced secretion and donor 4 displaying elevated levels compared to control DPSCs. Nonetheless, after differentiation, both CMT1A DPSC-SCs secreted comparable βNGF concentrations, which were consistently lower than those observed in the control DPSC-SCs (Fig. 5C). Contrary, GDNF concentrations showed no consistent pattern across lines. A decreasing trend was observed in control 1 and donor 3, while control 3 and donor 4 exhibited an increasing trend of GDNF secretion post-differentiation. Notably, within the DPSC-SC conditions, GDNF secretion in control 3 DPSC-SCs was significantly 16.45-fold elevated (P=0.0429) compared to the other control 1 DPSC-SC control group. Additionally, across both DPSC and DPSC-SC conditions, GDNF concentrations observed in control 1 and donor 4 were consistently lower than those observed in control 3 and donor 3, suggesting the absence of a clear disease-related pattern (Fig. 5D).

To further investigate the interaction between SCs and neurons, and to assess their basic compatibility in co-culture, a 24-well plate co-culture was established under four distinct conditions: (1) iPSC-MN in standard medium, (2) iPSC-MN in co-culture medium, (3) co-culture with control DPSC-SCs or (4) CMT1A-derived DPSC-SCs in co-culture medium. Given that SCs initiate the formation of myelin sheaths around axons while still undergoing differentiation, DPSC-SCs were added either during or after their differentiation process (11, 15). This design aimed to evaluate whether the timing of DPSC-SC introduction influences their ability to interact with iPSC-MNs. Brightfield microscopy revealed that iPSC-MN cultured in co-cultured medium remained viable and exhibited typical morphology, including organized soma clusters and extensive neurite networks, comparable to those observed in standard medium. Although soma boundaries were slightly less defined,

overall neuronal integrity was maintained, confirming the suitability of the co-culture medium. Additionally, in both conditions 3 and 4, iPSC-MN co-cultured with fully differentiated DPSC-SCs tended to consistently form rounded soma clusters and neurite networks, indicative of healthy iPSC-MN morphology. Whereas DPSC-SCs added during differentiation, similar network formation was observed, although increased neuronal cell death was occasionally noted, and soma clusters often tended to be less sharp. Moreover, CMT1A DPSC-SC showed indications of reduced survival. Lastly, DPSC-SCs introduced during their differentiation tended to remain spatially separated from iPSC-MNs more often in both conditions, whereas post-differentiation added DPSC-SCs showed greater spatial proximity to iPSC-MN in both cell lines. The findings suggest differences in neuron-SC interactions between control and CMT1A conditions (Fig. 5E).

Therefore, a compartmentalized co-culture system (XONA) was employed to study differential migration and interaction dynamics between iPSC-MN and either healthy or CMT1A fully differentiated DPSC-SCs. Prior to DPSC-SC addition, iPSC-MN somas were evenly distributed and axons broadly dispersed throughout the neuronal compartment. Several axons projected toward the microchannels, with occasional anchoring at the openings, and early network formation was observed. On D1, following DPSC-SC addition, a retraction artefact of iPSC-MN projections from the microchannel was noted, potentially caused by pipetting-related mechanical disturbance during SC seeding. Nevertheless, DPSC-SCs were evenly distributed within their compartment, extending up to the microchannel boundary. Importantly, at this stage, no iPSC-MN cell bodies, nor axons, nor any DPSC-SC had yet crossed the microchannels into the opposite compartment in either condition. Over time, distinct, condition-specific patterns of cell migration and axonal outgrowth emerged. In the control condition, DPSC-SCs began migrating through the microchannels into the neuronal compartment by D4, initially localizing in close proximity to the channel. Both the number of migrating cells and their migration depth increased progressively: on D15, several DPSC-SCs reached the mid-region, whereas on D28, the neuronal compartment was broadly populated with DPSC-SCs throughout its full length. In contrast, CMT1A-derived DPSC-SCs showed minimal migration throughout the entire period. Rare crossings were occasionally observed but remained limited in the immediate proximity of the channel, with the majority of DPSC-SCs staying confined to their original compartment, even at the endpoint. On the other hand, axonal outgrowth displayed the opposite pattern. In the CMT1A condition, iPSC-MN progressively extended axons into the SC compartment. By D4, short migrated axonal projections were observed near the channel exit. This axonal migration into the SC compartment increased by D15, forming initial networks near the channel, and intensified by D22, with dense axonal projections extending into mid- and distal regions. On D28, the SC compartment was extensively innervated, forming an interconnected axonal network. Contrary, such axonal invasion into the SC compartment was minimal to absent in the control condition. Across all time points, only a few axons occasionally crossed into the SC compartment, forming minuscule, localized projection networks near the channel without further extension (Fig. 5F).

Confocal microscopy of the XONA devices stained for the SC-marker S100β and neuronal marker Beta-3 Tubulin (βIIITUB) confirmed these observations by revealing pronounced migration of control DPSC-SCs into the neuronal compartment, accompanied by limited axonal extension into the SC compartment (Fig. 5G). In contrast, the CMT1A condition showed the opposite pattern, with minimal SC migration but robust axonal innervation of the SC compartment. (Fig. 5 H). Migration distances analysis showed that markedly fewer CMT1A DPSC-SCs migrated, representing 4.92-fold less frequently, compared to the control DPSC-SCs. Additionally, scatter plot analysis indicated that in the CMT1A condition, the few migrated SCs remained in close proximity to the channel. Contrary, in the control condition, DPSCs clustered near the close proximity of the channel (42.4%), reached the mid-compartment (42.4%), and a smaller subset even migrated toward the distal end (15.2%) (Fig. 5I).

***CMT1A DPSC-SCs* present reduced interaction with surrounding collagen type I in 3D hydrogels -** To assess the bidirectional interaction between SCs, neurons, and ECM, collagen type I-based hydrogels were generated containing iPSC-MN co-cultured with either CMT1A or control DPSC-SCs. Collagen organization was visualized by SHG confocal microscopy. Hydrogels with control DPSC-SCs

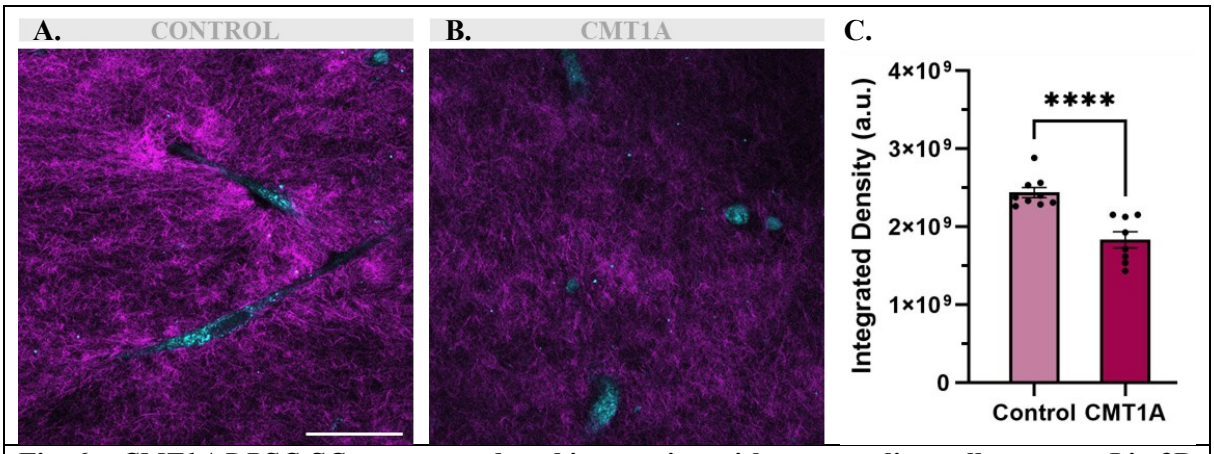

Fig. 6 – *CMT1A DPSC-SCs* present reduced interaction with surrounding collagen type I in 3D hydrogels. (A-B) Representative second harmonic generation confocal images of a 3D co-culture hydrogel containing iPSC-MNs with either **(A)** control or **(B)** CMT1A differentiated DPSC-SCs, showing collagen type I (magenta) and DPSC-SCs (cyan). Scale bar; 50 µm. **(C)** Corresponding quantification of integrated density per condition. Data is presented as mean ± SEM. ****P < 0,0001; one-way Mann-Whitney U test. *CMT1A; Charcot-Marie-Tooth Disease Type I.*

showed markedly increased collagen fluorescence intensity in regions immediately adjacent to and surrounding the SCs (Fig. 6A). Conversely, in hydrogels containing CMT1A DPSC-SCs, collagen fibers appeared uniformly distributed across the construct, including pericellular regions (Fig. 6B). Moreover, total integrated densities were significantly lower (P<0.0001; 1.3-fold) in the CMT1A condition compared to the control (Fig. 6C).

DISCUSSION

Schwann cell dysfunction is a key hallmark of CMT1A, contributing directly to impaired myelination and subsequent peripheral nerve degeneration (19). However, the characteristics and functional consequences of this dysfunction remain insufficiently understood. To address this gap, this study aimed to further elucidate SC pathology in the context of CMT1A. For this purpose, we employed our human *in vitro* model based on DPSCs, which have been previously demonstrated to successfully differentiate into DPSC-SCs (57, 58). Consistent with previous studies, efficient control DPSC-to-DPSC-SC differentiation was confirmed, as demonstrated by the acquisition of SC morphology and the upregulation of established SC markers, including S100β and CJUN (20, 57, 58, 68). Additionally, our findings validated that CMT1A DPSCs also retain effective differentiation capacity, as evidenced by consistent upregulation of the established SC marker LAM in both CMT1A and control DPSC-SCs (69). Subsequently, this study incorporated four independent DPSC lines derived from CMT1A patients alongside multiple controls. This is particularly relevant, given the well-documented clinical heterogeneity in CMT1, including differences in disease severity, age of onset, and progression (9, 64, 65, 70-72). Such variability has been underrepresented in previous CMT1A research. Particularly, iPSC-based studies often relied on a single patient-derived line, limiting their ability to reflect inter-patient diversity (55, 73). Similarly, transgenic CMT1A rodent models, typically generated through random multicopy insertions of *PMP22* cDNA, fail to capture the substantial genetic heterogeneity (35). Hence, our approach enabled us to investigate variability between donors in disease-relevant features. Particularly, our results showed a downward trend in *PMP22* mRNA expression upon differentiation in both CMT1A and control conditions. However, *PMP22* mRNA expression levels in CMT1A DPSC-SCs remained consistently lower than in controls, notwithstanding the additional *PMP22* copy. In contrast, PMP22 protein levels were elevated in DPSCs from nearly all CMT1A donors and remained high in all CMT1A DPSC-SCs, compared to control DPSC and DPSC-SCs, respectively. Remarkably, PMP22 mRNA and protein levels varied substantially across CMT1A donors, highlighting considerable inter-individual heterogeneity in expression. These observations align with previous reports from sural nerve and skin biopsies of CMT1A patients, which similarly demonstrated reduced PMP22 transcript levels and elevated protein expression,

marked with patient-to-patient variability (74, 75). Consequently, these findings not only support the notion that additional regulatory mechanisms, such as constitutional or temporal fluctuations in *PMP22* mRNA expression, may underly the observed discrepancies between patients (74). They also validate the model's ability to preserve key pathological features of CMT1A upon successful differentiation and underscore its utility for investigating inter-individual variation.

Previous research into CMT1A pathology has proposed the presence of an aberrant SC phenotype, with some reporting a shift toward a repair-like phenotype, and others pointing to impaired or incomplete differentiation along the Schwann cell lineage (75-77). In support of this notion, this study examined the temporal expression of two major regulators of SC differentiation, *OCT6* and *ERB3,* during key time points of this process (78, 79). Our results revealed that both control and CMT1A-derived cells exhibited similar temporal patterns of *OCT6* and *ERB3* up- and downregulation throughout the differentiation process. However, at certain crucial time points, differential expression levels were observed between CMT1A and control conditions. While these deviations may indicate subtle disruptions, further investigation is required to draw conclusions. Especially since another iPSC-based CMT1A study supported this possibility, which indicated that elevated *PMP22* expression may hinder SC differentiation. It was shown that neural crest stem cells either fail to generate SCs or become arrested at a promyelinating stage, leading to failed myelination despite transcribed myelin proteins (11). Taken together, these results underscore the importance of extending our approach by exploring a broader set of genes implicated in SC development. Hence, such experiments may enable pinpointing the specific stages at which differentiation is most affected and elucidate the disrupted transcriptional pathways in the formation of the aberrant SC phenotype in CMT1A. Nevertheless, our data provided further insights into the phenotypic variation of these disease SCs. Analysis of SC-related genes in CMT1A donors revealed marked variability in gene expression changes, both upon differentiation and between donors. The absence of a consistent expression pattern across donors suggests that each donor has a unique combination of alterations affecting genes involved in myelination, SC transcriptional regulation, and ECM-related genes, potentially driving the emergence of heterogeneous and dysfunctional SC phenotypes in CMT1A. For instance, *MPZ* was downregulated in donors 2 and 4, while donor 1 showed a pronounced reduction in *PLP1*. Both genes are essential constituents of the total peripheral myelin, and their downregulation may reflect impaired myelin formation (16, 80-82). Additionally, *OCT6*, a key regulator of peripheral myelination, was consistently reduced across all CMT1A DPSC-SCs compared to controls (83, 84). Collectively, these observations raise the possibility that each CMT1A patient harbours a distinct set of transcriptional alterations that compromise the myelinating capacity of SCs. In parallel, genes linked to immature or dedifferentiated SC states, such as $P75^{NTR}$, which was upregulated in donors 1 and 2, and *SOX2*, which showed elevated levels in donor 3 post-differentiation. Upregulation in these genes suggests a shift toward a less mature or dedifferentiated phenotype (68, 85). This observed combination of reduced myelin gene expressions and upregulation of immature or dedifferentiation-associated genes mirrors the transcriptional profile of repair SCs, also known as Büngner SCs, which are SCs that arise in response to peripheral nerve injury (25, 26, 68, 86). Therefore, these findings may indicate that SCs in CMT1A adopt a persistent repair-like state. Moreover, alterations in repair-associated genes were observed. *CJUN*, a transcription factor involved in the secretion of neurotrophic factors, was elevated in donors 2 and 3 (68, 87). *NCAM*, a marker linked to axon guidance, regeneration, and the pre-myelinating SC phase of Büngner SCs, showed increased expression in donors 2 and 4 (68, 88, 89). Additionally, all CMT1A lines exhibited reduced *LAM* expression, suggesting a diminished capacity to produce laminin-2, a key component of the basal lamina (90). These gene expression changes are known to play a pivotal role in promoting or maintaining the Büngner SCs (27, 68). Together, these findings support the notion that SCs in CMT1A display a persistent, injury-like state characterized by impaired myelination, myelin clearance, and incomplete maturation (26, 47, 68). Considering the potential phenotypic resemblances between SC phenotypes in CMT1A and those observed following peripheral nerve injury, future research should aim to systematically compare the molecular and functional alterations in CMT1A with the

established mechanisms governing peripheral nerve injury-induced repair. Such comparative analyses may uncover converging molecular pathways and regulatory disruptions, thereby offering novel insights into disease pathology.

To further characterize the proposed aberrant SC phenotypes and associated dysfunctions in CMT1A, this study investigated the neurotrophic factor secretion capacity of both DPSC and DPSC-SCs from CMT1A donors in comparison to normal controls. SC play a crucial paracrine function, continuously releasing low baseline levels of neurotrophic factors under physiological conditions to maintain proper nerve function, support axonal health, ensure effective nerve conduction, and preserve peripheral nerve integrity (3, 68). Accordingly, the consistent detection of BDNF, GDNF, NT3, and βNGF across all DPSCs and DPSC-SCs, including both CMT1A and control groups, confirms that a baseline neurotrophic secretory capacity was retained. This preservation of fundamental SC function further validates our *in vitro* model as a suitable platform for studying disease-associated SC phenotypes and their functions. Subsequently, among these factors, BDNF showed a marked increase following differentiation in most CMT1A donor lines, with levels from DPSC-SCs exceeding those observed in control DPSC-SCs. Normally, such upregulation of BDNF is typically induced by peripheral nerve injury as a repair response mediated by Büngner SCs (23-25, 27, 68). However, in the present study, only NRG-1 was present, which mimics axonal presence, but no injury-related cues were applied (91). Given that our results show this upregulation even in the absence of injury or external stimuli, it may indicate a constitutive and potentially aberrant activation of a repair-like phenotype in CMT1A. Of note, donor 3 exhibited a significant reduction in BDNF secretion upon differentiation, which may be attributable to previously observed downregulation of CJUN, a key regulator of BDNF expression in SCs (23, 26, 27). Conversely, donor 1 demonstrated increased BDNF secretion despite low CJUN levels, suggesting alternative regulatory mechanisms may be involved. Additionally, pathways such as STAT3 or elevated *NGF* mRNA, both known to be activated by peripheral nerve injury to regulate BDNF, may provide compensatory signaling to maintain neurotropic output (26, 92). Furthermore, NT3, another neurotrophic factor implicated in axonal growth after injury and synergistic with BDNF, but its expression levels are independently regulated (24). Despite a general decrease in NT3 levels following differentiation, overall concentrations remained comparable across CMT1A and control DPSC-SCs. Moreover, βNGF, essential for neurite outgrowth after nerve injury, showed consistent secretion across CMT1A DPSC-SCs, yet at lower levels than in control DPSC-SCs (92). Both NT3 and βNGF results may suggest the maintenance of a physiological, non-repair state-related secretion. Lastly, GDNF, primarily essential for neuronal survival, exhibited greater inter-donor variability (92). The donor-specific fluctuations in this neurotrophin concentration likely reflect the heterogeneous characteristics of CMT1A, possibly contributing to differential rates of axonal degeneration, SC phenotype instability, and regenerative failure. Collectively, the predominant increased secretion by CMT1A DPSC-SCS was limited to BDNF, consistent with the staggered temporal expression patterns of neurotrophic factors during peripheral nerve repair, with different neurotrophic factors being activated in a sequential rather than simultaneous manner (26, 92). Moreover, the observed heterogeneity in SC phenotypes may reflect disrupted regulation of neurotrophic factor secretion or may require a proper SC state, which may not be achieved in CMT1A (93). Hence, as the current literature lacks supporting evidence on neurotrophic factor secretion in the context of CMT1A, our findings warrant further validation. Given that neurotrophic factor secretion by SCs is strongly driven by nerve injury, future studies should investigate how CMT1A SCs respond to injury-related cues (23-27, 92). This is particularly relevant considering our findings suggest that these cells may already exhibit features of a repair-like phenotype in physiological conditions. For instance, incorporating injury-associated signals such as pro-inflammatory cytokines or axonal damage compounds into the culture system may help elucidate whether CMT1A SCs display an altered or inappropriate activation of neutrophic processes. Looking ahead, establishing an isogenic DPSC and DPSC-SC line could reduce variability among controls and strengthen future analyses, given the occasional inconsistencies observed between control samples.

To further elucidate SC-neuron interactions in CMT1A, we established a 24-well plate co-culture system using differentiating iPSC-MN and either differentiating or fully differentiated

DPSC-SCs from both a control donor and a CMT1A donor. This approach is particularly informative, as SCs are known to initiate myelin sheath formation during late differentiation stages (11, 15). When co-cultured with fully differentiated DPSC-SCs, iPSC-MNs displayed comparable viability and morphology across both control and CMT1A conditions, relative to iPSC-MNSs cultured alone. In contrast, co-cultures with still-differentiating DPSC-SCs were qualitatively associated with increased neuronal death and disrupted soma organization. This observation likely reflects the critical supportive role of mature SCs in promoting neuronal survival and maturation, consistent with the literature demonstrating that mature SCs enhance neuronal differentiation via neurotrophic factor secretion (94). This is in line with the previously observed BDNF upregulation in CMT1A DPSC-SC, which likely promotes more neuronal survival cues than immature DPSC-SCs (24). However, it diverges from the inconsistent expression patterns of other neurotrophic factors such as NT3 and βNGF in some CMT1A donors. Nevertheless, as discussed earlier, it remains to be clarified whether direct neuron-SC contact modulates the neurotrophic profile of CMT1A SCs. Notably, previous studies have shown that axonal signals can sustain the upregulation of neurotrophins like NT3 and CNTF in myelinating SCs, warranting further investigation in the CMT1A context (95-97). Collectively, these observations validate the suitability of the co-culture medium and the preference for using fully differentiated DPSC-SCs to ensure optimal neuronal survival. Moreover, the observed differences in SC-neuron interactions between control and CMT1A conditions highlight the necessity for further studies to elucidate mechanisms underlying SC dysfunction in CMT1A. Notably, CMT1A DPSC-SCs demonstrated reduced survival and spatial alignment with neurons. This aligns with our observations from the microfluidic co-culture experiment. In this setup, control DPSC-SCs showed active migration toward the neuronal compartment, suggestive of effective neuron-derived neuron-SC cue recognition and engagement. Contrary, CMT1A DPSC-SCs demonstrated minimal migratory activity, potentially reflecting an impaired ability to respond to neuronal-derived cues. These findings were corroborated by results from the 24-well plate co-culture, in which CMT1A DPSC-SCs demonstrated compromised alignment and spatial organization around motor neurons. These deficits may, at least in part, be explained by the downregulation of adhesion/ECM-related genes observed in our SC-gene expression analyses (98). Specifically, CMT1A DPSC-SCs exhibited reduced expression of *LAMA2A*, *LAMA4A*, and *NCAM* compared to control DPSC-SCs. *LAMA2A* is known to play a crucial role in SC-axon adhesion and migration, while LAMA4A facilitates SC-axon interaction, and *NCAM* is essential for cell-cell adhesion and communication between SC and axons (99-101). The reduced expression of these genes may compromise proper neuron-SC recognition, alignment, and adhesion, or impaired migratory or communication capabilities, as reflected in our functional observations. Notably, in the microfluidic system, axonal projections extended into the SC compartment under CMT1A conditions, an event not observed in the control setting. This aberrant projection pattern may reflect a compensatory neuronal response to deficient SC engagement. Moreover, a suggested contributing factor is the elevated secretion of BDNF observed in most CMT1A DPSC-SC lines. In response to peripheral nerve injury, BDNF secreted by the Büngner SCs promotes axonal elongation via TrkB receptor activation (24, 102, 103). Accordingly, the amplified secretion of BDNF by CMT1A DPSC-SCSs may promote axonal growth despite impaired structural or functional support. Future studies are warranted to functionally validate these observations. For instance, neurite outgrowth assay using conditioned medium from CMT1A DPSC-SCs could clarify whether enhanced axonal elongation is directly mediated by the secreted neurotrophic factors, including BDNF. In parallel, scratch migration assay could be employed to assess the intrinsic migratory capacity of DPSC-SCs across donors, and determine whether the reduced motility correlates with altered expression of adhesion- and ECM-related genes in CMT1A.

Finally, increasing evidence underscores the pivotal role of the ECM in regulating SC behavior and myelination. The ECM not only provides structural support but also mediates SC adhesion, migration, polarity, differentiation, and myelination via integrin-mediated signaling pathways *(*30, 31*)*. Hence, to investigate potential disruption in ECM engagement, we evaluated the bidirectional interactions between neurons, SCs, and ECM using a 3D collagen type I hydrogel. In

this system, CMT1A DPSC-SCs displayed diminished interaction with the surrounding collagen type I matrix compared to the control condition. This impaired matrix engagement may be linked to the reduced expression of *LAMA2A* observed in our earlier SC-gene experiment. *LAMA2A* encodes laminin-2, a key ECM protein essential for the formation of the basal lamina and for mediating SC anchorage to the extracellular environment (47, 99). The downregulation could compromise cell-matrix adhesion, necessary for proper SC alignment and myelination (21, 28-31, 69). These findings imply that DPSC-SCs under a healthy condition engage in a more active interaction with the surrounding collagen type I compared to those in the CMT1A condition. Hence, in light of increasing evidence for ECM involvement in CMT1A pathology, further research should seek to elucidate the specific role of ECM-SC interactions in driving SC dysfunction in CMT1A. For instance, future experiments could investigate whether disruptions in integrin expression or signaling contribute to impaired migration, differentiation, and myelination capacity of the aberrant CMT1A SCs. Should such impairments be confirmed, experimental restoration of integrin function may offer a potential strategy to rescue SC functionality. Moreover, culturing CMT1A DPSC-SCs on biomimetic scaffolds replicating normal ECM environments may reveal whether exogenous ECM cues are sufficient to restore key functions. Conversely, engineering CMT1A-like ECM substrates could help determine whether the pathological matrix itself actively impairs SC phenotypes, both in CMT1A and control DPSC-SCs.

CONCLUSION

In conclusion, this study validated the use of a patient-derived *in vitro* model in which CMT1A-derived DPSC can successfully differentiate into DPSC-SCs while retaining key pathological features of CMT1A. This model enabled the investigation of inter-individual variability and CMT1A-related disease mechanisms. Through this approach, we identified a heterogeneous yet converging aberrant SC phenotype across donors, ultimately suggesting the adoption of a persistent, repair-like state. Additionally, impairments in neurotrophic signaling, SC-neuron interactions, and SC-ECM interactions were observed, which are likely contributors to the SC dysfunction in CMT1A.

REFERENCES

1. Nagappa M, Sharma S, Taly AB. Charcot-Marie-Tooth Disease. StatPearls [Internet]: StatPearls Publishing; 2024.
2. Nam SH, Choi B-O. Clinical and genetic aspects of Charcot-Marie-Tooth disease subtypes. Precision and Future Medicine. 2019;3(2):43-68.
3. Morena J, Gupta A, Hoyle JC. Charcot-Marie-Tooth: from molecules to therapy. International journal of molecular sciences. 2019;20(14):3419.
4. Bird TD. Charcot-Marie-Tooth hereditary neuropathy overview. 2022.
5. Dong H, Qin B, Zhang H, Lei L, Wu S. Current Treatment Methods for Charcot–Marie–Tooth Diseases. Biomolecules. 2024;14(9):1138.
6. Fridman V, Saporta MA. Mechanisms and treatments in demyelinating CMT. Neurotherapeutics. 2021;18(4):2236-68.
7. Bolino A, D'Antonio M. Recent advances in the treatment of Charcot-Marie-Tooth neuropathies. Journal of the Peripheral Nervous System. 2023;28(2):134-49.
8. Okamoto Y, Takashima H. The current state of Charcot–Marie–Tooth disease treatment. Genes. 2023;14(7):1391.
9. Saporta A, Sottile S, Miller L. Charcot Marie Tooth (CMT) Subtypes and Genetic Testing Strategies Ann Neurol. Press This manuscript provides algorithms for genetic testing in CMT based on more than.1000.
10. Manganelli F, Tozza S, Pisciotta C, Bellone E, Iodice R, Nolano M, et al. Charcot-Marie-Tooth disease: frequency of genetic subtypes in a Southern Italy population. Journal of the Peripheral Nervous System. 2014;19(4):292-8.
11. Clayton BL, Allan KC, Nevin ZS, Elitt MS, Tesar PJ. Disorders of myelin. Neurodevelopmental Disorders: Elsevier; 2020. p. 309-35.
12. Bernard R, Boyer A, Nègre P, Malzac P, Latour P, Vandenberghe A, et al. Prenatal detection of the 17p11. 2 duplication in Charcot-Marie-Tooth disease type 1A: necessity of a multidisciplinary approach for heterogeneous disorders. European Journal of Human Genetics. 2002;10(5):297-302.
13. Boutary S, Echaniz-Laguna A, Adams D, Loisel-Duwattez J, Schumacher M, Massaad C, et al. Treating PMP22 gene duplication-related Charcot-Marie-Tooth disease: the past, the present and the future. Translational Research. 2021;227:100-11.

14. Pantera H, Shy ME, Svaren J. Regulating PMP22 expression as a dosage sensitive neuropathy gene. Brain research. 2020;1726:146491.
15. Taveggia C, Feltri ML, Wrabetz L. Signals to promote myelin formation and repair. Nature Reviews Neurology. 2010;6(5):276-87.
16. Li J, Parker B, Martyn C, Natarajan C, Guo J. The PMP22 gene and its related diseases. Molecular neurobiology. 2013;47:673-98.
17. Maier M, Castagner F, Berger P, Suter U. Distinct elements of the peripheral myelin protein 22 (PMP22) promoter regulate expression in Schwann cells and sensory neurons. Molecular and Cellular Neuroscience. 2003;24(3):803-17.
18. Rudnik-Schöneborn S, Auer-Grumbach M, Senderek J. Charcot-Marie-Tooth disease and hereditary motor neuropathies–Update 2020. Medizinische Genetik. 2020;32(3):207-19.
19. Robaglia-Schlupp A, Pizant J, Norreel JC, Passage E, Saberan-Djoneidi D, Ansaldi JL, et al. PMP22 overexpression causes dysmyelination in mice. Brain. 2002;125(10):2213-21.
20. Woodhoo A, Sommer L. Development of the Schwann cell lineage: from the neural crest to the myelinated nerve. Glia. 2008;56(14):1481-90.
21. Fornaro M, Marcus D, Rattin J, Goral J. Dynamic environmental physical cues activate mechanosensitive responses in the repair Schwann cell phenotype. Cells. 2021;10(2):425.
22. Bosch-Queralt M, Fledrich R, Stassart RM. Schwann cell functions in peripheral nerve development and repair. Neurobiol Dis. 2023;176(105952):10.1016.
23. Arthur-Farraj P, Coleman MP. Lessons from injury: How nerve injury studies reveal basic biological mechanisms and therapeutic opportunities for peripheral nerve diseases. Neurotherapeutics. 2021;18(4):2200-21.
24. Fu H, Hu D, Chen J, Wang Q, Zhang Y, Qi C, et al. Repair of the injured spinal cord by schwann cell transplantation. Frontiers in Neuroscience. 2022;16:800513.
25. Jiang M, Chen M, Liu N. Interactions between Schwann cell and extracellular matrix in peripheral nerve regeneration. Frontiers in Neurology. 2024;15:1372168.
26. Jessen KR, Mirsky R. The success and failure of the Schwann cell response to nerve injury. Frontiers in cellular neuroscience. 2019;13:33.
27. Xu Z, Orkwis JA, DeVine BM, Harris GM. Extracellular matrix cues modulate Schwann cell morphology, proliferation, and protein expression. Journal of Tissue Engineering and Regenerative Medicine. 2020;14(2):229-42.
28. Chernousov MA, Yu WM, Chen ZL, Carey DJ, Strickland S. Regulation of Schwann cell function by the extracellular matrix. Glia. 2008;56(14):1498-507.
29. Berti C, Nodari A, Wrabetz L, Feltri ML. Role of integrins in periphral nerves and hereditary neuropathies. Neuromolecular medicine. 2006;8:191-204.
30. Nodari A, Zambroni D, Quattrini A, Court FA, D'Urso A, Recchia A, et al. β1 integrin activates Rac1 in Schwann cells to generate radial lamellae during axonal sorting and myelination. The Journal of cell biology. 2007;177(6):1063-75.
31. Fernandez-Valle C, Gwynn L, Wood PM, Carbonetto S, Bunge MB. Anti-β1 integrin antibody inhibits schwann cell meylination. Journal of neurobiology. 1994;25(10):1207-26.
32. Palumbo C, Massa R, Panico M, Di Muzio A, Sinibaldi P, Bernardi G, et al. Peripheral nerve extracellular matrix remodeling in Charcot-Marie-Tooth type I disease. Acta neuropathologica. 2002;104:287-96.
33. Suter U, Scherer SS. Disease mechanisms in inherited neuropathies. Nature reviews neuroscience. 2003;4(9):714-26.
34. Feltri ML, Porta DG, Previtali SC, Nodari A, Migliavacca B, Cassetti A, et al. Conditional disruption of β1 integrin in Schwann cells impedes interactions with axons. Journal of Cell Biology. 2002;156(1):199-210.
35. Juneja M, Burns J, Saporta MA, Timmerman V. Challenges in modelling the Charcot-Marie-Tooth neuropathies for therapy development. Journal of Neurology, Neurosurgery & Psychiatry. 2019;90(1):58-67.
36. De Grado A, Serio M, Saveri P, Pisciotta C, Pareyson D. Charcot-marie-tooth disease: a review of clinical developments and its management-What's new in 2025? Expert Review of Neurotherapeutics. 2025(just-accepted).
37. Yoshioka Y, Taniguchi JB, Homma H, Tamura T, Fujita K, Inotsume M, et al. AAV-mediated editing of PMP22 rescues Charcot-Marie-Tooth disease type 1A features in patient-derived iPS Schwann cells. Communications Medicine. 2023;3(1):170.
38. Pisciotta C, Saveri P, Pareyson D. Updated review of therapeutic strategies for Charcot-Marie-Tooth disease and related neuropathies. Expert review of neurotherapeutics. 2021;21(6):701-13.

39. Stavrou M, Kleopa KA. CMT1A current gene therapy approaches and promising biomarkers. Neural regeneration research. 2023;18(7):1434-40.
40. Robertson A, Perea J, McGuigan A, King R, Muddle J, Gabreëls-Festen A, et al. Comparison of a new pmp22 transgenic mouse line with other mouse models and human patients with CMT1A. Journal of anatomy. 2002;200(4):377-90.
41. Sereda MW, Nave K-A. Animal models of Charcot-Marie-Tooth disease type 1A. Neuromolecular medicine. 2006;8:205-15.
42. Stratton JA, Kumar R, Sinha S, Shah P, Stykel M, Shapira Y, et al. Purification and characterization of schwann cells from adult human skin and nerve. Eneuro. 2017;4(3).
43. Moss KR, Mi R, Kawaguchi R, Ehmsen JT, Shi Q, Vargas PI, et al. hESC-and hiPSC-derived Schwann cells are molecularly comparable and functionally equivalent. Iscience. 2024;27(6).
44. Aparicio GI, Monje PV. Human Schwann cells in vitro I. Nerve Tissue Processing, Pre-degeneration, Isolation, and Culturing of Primary Cells. Bio-protocol. 2023;13(22):e4748.
45. Shojapour M, Mosayebi G, Hajihossein R, Noorbakhsh F, Mokarizadeh A, Ghahremani MH. A simplified protocol for the purification of schwann cells and exosome isolation from C57BL/6 mice. Reports of Biochemistry & Molecular Biology. 2018;7(1):9.
46. Monje PV. Human Schwann Cells in vitro II. Passaging, Purification, Banking, and Labeling of Established Cultures. Bio-protocol. 2023;13(22):e4882.
47. Andersen ND, Srinivas S, Piñero G, Monje PV. A rapid and versatile method for the isolation, purification and cryogenic storage of Schwann cells from adult rodent nerves. Scientific Reports. 2016;6(1):31781.
48. Kvigstad EF, Øverland IK, Skedsmo FS, Jäderlund KH, Gröndahl G, Hanche-Olsen S, et al. Cultivation of Schwann cells from fresh and non-fresh adult equine peripheral nerves. Journal of Neuroscience Methods. 2024;403:110054.
49. Li L, Chao J, Shi Y. Modeling neurological diseases using iPSC-derived neural cells: iPSC modeling of neurological diseases. Cell and tissue research. 2018;371:143-51.
50. Paik DT, Chandy M, Wu JC. Patient and disease–specific induced pluripotent stem cells for discovery of personalized cardiovascular drugs and therapeutics. Pharmacological reviews. 2020;72(1):320-42.
51. Cerneckis J, Cai H, Shi Y. Induced pluripotent stem cells (iPSCs): molecular mechanisms of induction and applications. Signal Transduction and Targeted Therapy. 2024;9(1):112.
52. Van Lent J, Verstraelen P, Asselbergh B, Adriaenssens E, Mateiu L, Verbist C, et al. Induced pluripotent stem cell-derived motor neurons of CMT type 2 patients reveal progressive mitochondrial dysfunction. Brain. 2021;144(8):2471-85.
53. Mukherjee-Clavin B, Mi R, Kern B, Choi IY, Lim H, Oh Y, et al. Comparison of three congruent patient-specific cell types for the modelling of a human genetic Schwann-cell disorder. Nature biomedical engineering. 2019;3(7):571-82.
54. Shi L, Huang L, He R, Huang W, Wang H, Lai X, et al. Modeling the pathogenesis of Charcot-Marie-Tooth disease type 1A using patient-specific iPSCs. Stem Cell Reports. 2018;10(1):120-33.
55. Van Lent J, Prior R, Pérez Siles G, Cutrupi AN, Kennerson ML, Vangansewinkel T, et al. Advances and challenges in modeling inherited peripheral neuropathies using iPSCs. Experimental & molecular medicine. 2024;56(6):1348-64.
56. Yamanaka S. Pluripotent stem cell-based cell therapy—promise and challenges. Cell stem cell. 2020;27(4):523-31.
57. Libberecht K, Dirkx N, Vangansewinkel T, Vandendries W, Lambrichts I, Wolfs E. The Influence of Lysosomal Stress on Dental Pulp Stem Cell-Derived Schwann Cells. Biomolecules. 2024;14(4):405.
58. Martens W, Sanen K, Georgiou M, Struys T, Bronckaers A, Ameloot M, et al. Human dental pulp stem cells can differentiate into Schwann cells and promote and guide neurite outgrowth in an aligned tissue-engineered collagen construct in vitro. The FASEB Journal. 2014;28(4):1634.
59. Gronthos S, Mankani M, Brahim J, Robey PG, Shi S. Postnatal human dental pulp stem cells (DPSCs) in vitro and in vivo. Proceedings of the National Academy of Sciences. 2000;97(25):13625-30.
60. Hilkens P, Gervois P, Fanton Y, Vanormelingen J, Martens W, Struys T, et al. Effect of isolation methodology on stem cell properties and multilineage differentiation potential of human dental pulp stem cells. Cell and tissue research. 2013;353(1):65-78.

61. Gronthos S, Brahim J, Li W, Fisher L, Cherman N, Boyde A, et al. Stem cell properties of human dental pulp stem cells. Journal of dental research. 2002;81(8):531-5.
62. Tatullo M, Marrelli M, Shakesheff KM, White LJ. Dental pulp stem cells: function, isolation and applications in regenerative medicine. Journal of tissue engineering and regenerative medicine. 2015;9(11):1205-16.
63. Tiscornia G, Vivas EL, Belmonte JCI. Diseases in a dish: modeling human genetic disorders using induced pluripotent cells. Nature medicine. 2011;17(12):1570-6.
64. Colomban C, Micallef J, Lefebvre M-N, Dubourg O, Gonnaud P-M, Stojkovic T, et al. Clinical spectrum and gender differences in a large cohort of Charcot–Marie–Tooth type 1A patients. Journal of the Neurological Sciences. 2014;336(1-2):155-60.
65. Carvalho AA, Vital A, Ferrer X, Latour P, Lagueny A, Brechenmacher C, et al. Charcot-Marie-Tooth disease type 1A: clinicopathological correlations in 24 patients. Journal of the Peripheral Nervous System. 2005;10(1):85-92.
66. Struys T, Moreels M, Martens W, Donders R, Wolfs E, Lambrichts I. Ultrastructural and immunocytochemical analysis of multilineage differentiated human dental pulp-and umbilical cord-derived mesenchymal stem cells. Cells Tissues Organs. 2011;193(6):366-78.
67. Guo W, Naujock M, Fumagalli L, Vandoorne T, Baatsen P, Boon R, et al. HDAC6 inhibition reverses axonal transport defects in motor neurons derived from FUS-ALS patients. Nature communications. 2017;8(1):861.
68. Sardella-Silva G, Mietto BS, Ribeiro-Resende VT. Four seasons for schwann cell biology, revisiting key periods: Development, homeostasis, repair, and aging. Biomolecules. 2021;11(12):1887.
69. Scarpini E, Meola G, Baron P, Beretta S, Velicogna M, Scarlato G. S-100 protein and laminin: immunocytochemical markers for human Schwann cells in vitro. Experimental neurology. 1986;93(1):77-83.
70. Tao F, Beecham GW, Rebelo AP, Blanton SH, Moran JJ, Lopez-Anido C, et al. Modifier gene candidates in Charcot-Marie-Tooth disease type 1A: a case-only genome-wide association study. Journal of neuromuscular diseases. 2019;6(2):201-11.
71. Wu R, Lv H, Zhang W, Wang Z, Zuo Y, Liu J, et al. Clinical and pathological variation of Charcot-Marie-tooth 1A in a large Chinese cohort. BioMed Research International. 2017;2017(1):6481367.
72. Nam SH, Kanwal S, Lee MH, Kang TH, Jung S-C, Choi B-O, et al. Association of miR-149 polymorphism with onset age and severity in Charcot–Marie–Tooth disease type 1A. Neuromuscular Disorders. 2018;28(6):502-7.
73. Brunner JW, Lammertse HC, van Berkel AA, Koopmans F, Li KW, Smit AB, et al. Power and optimal study design in iPSC-based brain disease modelling. Molecular Psychiatry. 2023;28(4):1545-56.
74. Katona I, Wu X, Feely SM, Sottile S, Siskind CE, Miller LJ, et al. PMP22 expression in dermal nerve myelin from patients with CMT1A. Brain. 2009;132(7):1734-40.
75. Hanemann CO, Gabreëls-Festen AA, Stoll G, Müller HW. Schwann cell differentiation in Charcot-Marie-Tooth disease type 1A (CMT1A): normal number of myelinating Schwann cells in young CMT1A patients and neural cell adhesion molecule expression in onion bulbs. Acta neuropathologica. 1997;94:310-5.
76. Hanemann CO, Müller HW. Pathogenesis of Charcot–Marie–Tooth 1A (CMT1A) neuropathy. Trends in neurosciences. 1998;21(7):282-6.
77. Hanemann CO, Gabreëls-Festen AA, Müller HW, Stoll G. Low affinity NGF receptor expression in CMT1 A nerve biopsies of different disease stages. Brain. 1996;119(5):1461-9.
78. Liu Z, Jin Y-Q, Chen L, Wang Y, Yang X, Cheng J, et al. Specific marker expression and cell state of Schwann cells during culture in vitro. PloS one. 2015;10(4):e0123278.
79. Garratt AN, Voiculescu O, Topilko P, Charnay P, Birchmeier C. A dual role of erbB2 in myelination and in expansion of the schwann cell precursor pool. The Journal of cell biology. 2000;148(5):1035-46.
80. Berndt JA, Kim JG, Hudson LD. Identification of cis-regulatory elements in the myelin proteolipid protein (PLP) gene. Journal of Biological Chemistry. 1992;267(21):14730-7.
81. Nelis E, Haites N, Van Broeckhoven C. Mutations in the peripheral myelin genes and associated genes in inherited peripheral neuropathies. Human mutation. 1999;13(1):11-28.
82. Greenfield S, Brostoff S, Eylar E, Morell P. Protein composition of myelin of the peripheral nervous system. Journal of neurochemistry. 1973;20(4):1207-16.
83. Jagalur NB, Ghazvini M, Mandemakers W, Driegen S, Maas A, Jones EA, et al.

Functional dissection of the Oct6 Schwann cell enhancer reveals an essential role for dimeric Sox10 binding. Journal of Neuroscience. 2011;31(23):8585-94.
84. Stolt CC, Wegner M. Schwann cells and their transcriptional network: Evolution of key regulators of peripheral myelination. Brain Research. 2016;1641:101-10.
85. Roberts S. The control of Schwann cell myelination during development and after nerve injury. 2016.
86. Arthur-Farraj PJ, Latouche M, Wilton DK, Quintes S, Chabrol E, Banerjee A, et al. c-Jun reprograms Schwann cells of injured nerves to generate a repair cell essential for regeneration. Neuron. 2012;75(4):633-47.
87. Jessen K, Mirsky R. The repair Schwann cell and its function in regenerating nerves. The Journal of physiology. 2016;594(13):3521-31.
88. Silver J, Rutishauser U. Guidance of optic axons in vivo by a preformed adhesive pathway on neuroepithelial endfeet. Dev Biol. 1984;106(2):485-99.
89. Roche PH, Figarella-Branger D, Daniel L, Bianco N, Pellet W, Pellissier JF. Expression of cell adhesion molecules in normal nerves, chronic axonal neuropathies and Schwann cell tumors. J Neurol Sci. 1997;151(2):127-33.
90. Tohyama K, Ide C. The localization of laminin and fibronectin on the Schwann cell basal lamina. Arch Histol Jpn. 1984;47(5):519-32.
91. Birchmeier C, Nave KA. Neuregulin-1, a key axonal signal that drives Schwann cell growth and differentiation. Glia. 2008;56(14):1491-7.
92. Frostick SP, Yin Q, Kemp GJ. Schwann cells, neurotrophic factors, and peripheral nerve regeneration. Microsurgery: Official Journal of the International Microsurgical Society and the European Federation of Societies for Microsurgery. 1998;18(7):397-405.
93. Nobbio L, Fiorese F, Vigo T, Cilli M, Gherardi G, Grandis M, et al. Impaired expression of ciliary neurotrophic factor in Charcot-Marie-Tooth type 1A neuropathy. Journal of Neuropathology & Experimental Neurology. 2009;68(5):441-55.
94. Razavi S, Razavi MR, Kheirollahi-Kouhestani M, Mardani M, Mostafavi FS. Co-culture with neurotrophic factor secreting cells induced from adipose-derived stem cells: promotes neurogenic differentiation. Biochemical and Biophysical Research Communications. 2013;440(3):381-7.
95. Sahenk Z, Nagaraja HN, McCracken BS, King WM, Freimer ML, Cedarbaum JM, et al. NT-3 promotes nerve regeneration and sensory improvement in CMT1A mouse models and in patients. Neurology. 2005;65(5):681-9.
96. Sahenk Z, Galloway G, Clark KR, Malik V, Rodino-Klapac LR, Kaspar BK, et al. AAV1.NT-3 gene therapy for charcot-marie-tooth neuropathy. Mol Ther. 2014;22(3):511-21.
97. Lee DA, Zurawel, R. H., & Windebank, A. J. . Ciliary neurotrophic factor expression in Schwann cells is induced by axonal contact. Journal of neurochemistry. 1995;65(2), 564-568.
98. Wilson ER, Della-Flora Nunes G, Weaver MR, Frick LR, Feltri ML. Schwann cell interactions during the development of the peripheral nervous system. Dev Neurobiol. 2021;81(5):464-89.
99. Uziyel Y, Hall S, Cohen J. Influence of laminin-2 on Schwann cell–axon interactions. Glia. 2000;32(2):109-21.
100. Motta CMM, Endres KJ, Wesdemiotis C, Willits RK, Becker ML. Enhancing Schwann cell migration using concentration gradients of laminin-derived peptides. Biomaterials. 2019;218:119335.
101. Rutishauser U, Acheson, A., Hall, A. K., Mann, D. M., & Sunshine, J. . The neural cell adhesion molecule (NCAM) as a regulator of cell-cell interactions. Science, 240(4848), 53-57. 1988.
102. Dong Q, Ji YS, Cai C, Chen ZY. LIM kinase 1 (LIMK1) interacts with tropomyosin-related kinase B (TrkB) and Mediates brain-derived neurotrophic factor (BDNF)-induced axonal elongation. J Biol Chem. 2012;287(50):41720-31.
103. Wang Y, Liang J, Xu B, Yang J, Wu Z, Cheng L. TrkB/BDNF signaling pathway and its small molecular agonists in CNS injury. Life Sci. 2024;336:122282.

Acknowledgements – I'm grateful for Prof. Dr. Wolfs E. for welcoming me to her research team and providing me with this incredibly and exciting opportunity. Special thanks go to my supervisor Nathalie Dirkx for her daily supervision, guidance, support, expertise in research methods, relevant feedback, and enthusiasm. I would also like to thank all members of the FIERCE research group and fellow students for giving me additional assistance, support, and knowledge.

Author contributions – N.D. and E.W. conceived and designed the research. N.D. supervised the senior internship. N.D. and S.V.D.V. and performed the experiments. S.V.D.V. performed data analysis and wrote the thesis proofread by N.D. All authors carefully edited the manuscript.

Note – This thesis is grammatically supported by Gen AI.

SUPPORTING INFORMATION

Table S1 – CMT1A donor information.

Gender	Age
Donor 1	
Male	23 y/o
Donor 2	
Female	18 y/o
Donor 3	
Male	63 y/o
Donor 4	
Female	17 y/o

Abbreviations are listed in Table S5.

Table S2 – Composition of all culture and differentiation media.

(A) DPSC and DPSC-SC media

Component	Concentration/Factor
DPSC medium	
MEM Alpha Modification (αMEM)	90%
Heat inactivated Fetal Calf Serum (hiFCS)	10%
DPSC-to-SC differentiation medium D1	
αMEM	100%
β-mercaptoethanol (BME)	1 mM
DPSC-to-SC differentiation medium D2	
αMEM	90%
hiFCS	10%
Trans-retinoic acid (tRA)	35 ng/mL
DPSC-to-SC differentiation medium D≥5 = DPSC-SC medium	
αMEM	90%
hiFCS	10%
Neuregulin 1 (NRG1)	1 ng/mL
Forskolin	0.5 ng/mL
Fibroblast growth factor 2 (FGF2)	0.1 ng/mL
Platelet-derived growth factor (PDGF)	0.1 ng/mL
DPSC ELISA medium	
αMEM	98%
hiFCS	2%
DPSC-SC ELISA medium	
αMEM	98%
hiFCS	2%
NRG1	1 ng/mL
Forskolin	0.5 ng/mL
FGF2	0.1 ng/mL
PDGF	0.1 ng/mL

(B) iPSC and iPSC-MN media

Component	Concentration/Factor
iPSC medium	
Essential™ 8 medium	100%
Penicillin/streptomycin	1000 U/mL

(C) 24-well co-culture

Component	Concentration/Factor
Condition 1	
DMEM/F12	50%
Neurobasal	50%
Penicillin/streptomycin	100X
N2	100X
B27 -/-Vit.A	50X
BME	0.1%
Acid Ascorbic	0.5 µM
Glutamax	1%
BDNF	10 ng/mL
GDNF	10 ng/mL
CNTF	10 ng/mL
DAPT	20 µM
Condition 2, 3, and 4	
Condition 1 medium	50%
DMEM/F12	50%
Neurobasal	100X
Penicillin/streptomycin	100X
N2	50X
B27 -/-Vit.A	0.1%
BME	0.5 µM
Acid Ascorbic	1%
Glutamax	10 ng/mL
BDNF	10 ng/mL
GDNF	10 ng/mL
CNTF	20 µM
Forskolin	0.5 ng/mL
Fibroblast growth factor 2 (FGF2)	0.1 ng/mL
Platelet-derived growth factor (PDGF)	0.1 ng/mL

(D) XONA

Component	Concentration/Factor
iPSC wells	
DMEM/F12	50%
Neurobasal	50%
Penicillin/streptomycin	100X
N2	100X
B27 -/-Vit.A	50X
BME	0.1%
Acid Ascorbic	0.5 µM
Glutamax	1%
BDNF	10 ng/mL
GDNF	10 ng/mL
CNTF	10 ng/mL
DAPT	20 µM

SC wells	
MEM Alpha Modification (αMEM)	90%
Heat inactivated Fetal Calf Serum (hiFCS)	10%
NRG1	1 ng/mL
Forskolin	0.5 ng/mL
FGF2	0.1 ng/mL
PDGF	0.1 ng/mL

(E) Hydrogel

Hydrogel	
Condition 1 medium	50%
DMEM/F12	50%
Neurobasal	100X
Penicillin/streptomycin	100X
N2	50X
B27 -/-Vit.A	0.1%
BME	0.5 µM
Acid Ascorbic	1%
Glutamax	10 ng/mL
BDNF	10 ng/mL
GDNF	10 ng/mL
CNTF	20 µM
Forskolin	1 ng/mL
FGF2	0.2 ng/mL
PDGF	0.2 ng/mL

Abbreviations are listed in Table S5.

Table S3 – List of human primer sequences used for qPCR. Both Forward and Reversed sequences are (5'-3').

Gene transcript target	Full name	Primer sequences
PMP22	Peripheral Myelin protein 2	Forward: GGCAATGGACACGCAACTGATC Reversed: TGATCGACAGGATCATGGTGGC
P75NTR	Neurotrophin Receptor P75	Forward: AGTTGGACTGATTGTGGGTGT Reversed: CAGGCACAAGGGCTTCTTTTT
S100β	S100 Calcium Binding Protein B	Forward: GGAAGGGGTGAGACAAGG Reversed: GGTGGAAAACGTCGATGAG
SOX10	SRY-Box Transcription Factor 10	Forward: CCAGGCCCACTACAAGAGC Reversed: GGCTCTGGCCTGAGGGG
SOX2	SRY-Box Transcription Factor 10	Forward: CTCGGACTTGACCACCGAAC Reversed: GACCAGCTCGCAGACCTACA
LAMA2A	Laminin Subunit Alpha 2	Forward: TGAGTATGAAAGCAAGGCCAGA Reversed: TGGTAACACCAACATAATCGGG
LAMA4A	Laminin Subunit Alpha 4	Forward: CAGTGTAACCGGAGAATGCTTG Reversed: GACGCACTTATCACAGCTTATGG
MPZ	Myelin Protein Zero	Forward: GAGGAGGCTCAGTGCTATGG Reversed: TTCTGCTGTGGTCCAGCATT
PLP1	Proteolipid Protein 1	Forward: ACCTATGCCCTGACCGTTG Reversed: TGCTGGGGAAGGCAATAGACT
GFAP	Glial Fibrillary Acid Protein	Forward: ACCAGGACCTGCTCAATGTC Reversed: AAGGTCTGCACGGGAATG
SLUG	Snail Family Transcriptional Repressor 1	Forward: CGAACTGGACACACATACAGTG Reversed: CTGAGGATCTCTGGTTGTGGT
OCT6	POU Class 3 Homeobox 1	Forward: GCAGTTGCAGAATGGTGAGA Reversed: TGTAGCCATCCACACAAGGA
KROX20	Early Growth Response Protein 2	Forward: CCACGTCGGTGACCATCTTT Reversed: TTGATCATGCCATCTCCGGC
NCAM	Neural Cell Adhesion Molecule	Forward: GCCTGAAGCCCGAAACAAC Reversed: TGGGTTCCCCTTGGACTGG
CJUN	Jun Proto-Oncogene, AP-1 Transcription Factor Subunit	Forward: ACGGCGGTAAAGACCAGAAG Reversed: CTCGCCCAAGTTCAACAACC
L1CAM	L1 Cell Adhesion Molecule	Forward: TCGCCCTATGTCCACTACACCT Reversed: ATCCACAGGGTTCTTCTCTGGG
PAX3	Paired Box Gene 3	Forward: GGCTTTCAACCATCTCATTCCCG Reversed: GTTGAGGTCTGTGAACGGTGCT
ERB3	Erb-B2 Receptor Tyrosine Kinase 3	Forward: CTATGAGGCGATACTTGGAACGG Reversed: GCACAGTTCCAAAGACACCCGA
PGK1	Phosphoglycerate Kinase 1	Forward: CTGGGCAAGGATGTTCTGTT Reversed: GCATCTTTTCCCTTCCCTTC

Table S4 – List of primary and secondary antibodies used in immunocytochemistry, confocal microscopy, and Western Blotting.

(A) Primary antibodies

Target	Host species	Manufacturer	Reference number	Isotype	Dilution
S100β	Rabbit	Dako	Z0311	IgG	ICC: 1/350 Confocal: 1/300
$P75^{NTR}$	Mouse	Santa Cruz	sc-271708	IgG	ICC: 1/400
CJUN	Mouse	Santa Cruz	Sc-166540	IgG	ICC: 1/200
PMP22	Mouse	Origene	TA808964	IgG	ICC: 1/200 WB: 1/150
LAM1+2	Rabbit	Abcam	AB7463	IgG	ICC: 1/400
βIIITUB	Mouse	Sigma-Aldrich Chemie	T8578-200UL	IgG	Confocal: 1/200
GAPDH	Mouse	Santa Cruz	Sc-365062	IgG	WB: 1/1000

(B) Secondary antibodies

Target	Host species	Conjugate	Manufacturer	Reference number	Isotype	Dilution
Anti-Mouse	Goat	AF488	Invitrogen	A11017	IgG	Confocal: 1/500
Anti-Mouse	Goat	AF647	Invitrogen	A21235	IgG	ICC: 1/500
Anti-Mouse	Goat	AF555	Invitrogen	A21425	IgG	ICC: 1/500
Anti-Rabbit	Goat	AF555	Invitrogen	A21430	IgG	ICC: 1/500 Confocal: 1/500
Anti-Rabbit	Goat	AF647	Invitrogen	A21245	IgG	ICC: 1/500
Anti-Mouse	Goat	Immunoglobulins /HRP	Agilent Technologies	P0260	IgG	WB: 1/1000

Abbreviations are listed in Table S5.

Table S5 – List of abbreviations.

CMT1A – Charcot-Marie-Tooth disease type 1
DPSC – Dental pulp stem cells
DPSC-SC – dental pulp stem cell-derived Schwann cell
iPSC-MN – induced pluripotent stem cell-derived motor neuron
P75^{NTR} - P75 Neurotrophic Receptor
CJUN - Jun Proto-Oncogene AP-1 Transcription Factor Subunit
LAM - Laminin
LAMA2A - Laminin Subunit Alpha 2
LAMA4A - Laminin Subunit Alpha 2
PMP22 - Peripheral Myelin protein 2
PGK1 – Phosphoglycerate Kinase 1
MPZ – Myelin Protein Zero
PLP1 - Proteolipid Protein 1
S100β - S100 Calcium-Binding Protein B
SOX2 - SRY-Box Transcription Factor 2
SOX10 - SRY-Box Transcription Factor 10
KROX20 - Early Growth Response Protein 2
OCT6 - POU Class 3 Homeobox 1
CJUN - Jun Proto-Oncogene, AP-1 Transcription Factor Subunit
SLUG - Snail Family Transcriptional Repressor 1
ERB3 - Erb-B2 Receptor Tyrosine Kinase 3
GAPDH - Glyceraldehyde-3-fosfaatdehydrogenase
kDa - kilodalton
ECM – Extracellular Matrix
BDNF - Brain-Derived Neurotrophic Factor
GDNF - Glial Cell Line-derived Neurotrophic Factor
NT3 - Neurotrophin 3
βNGF - Beta Nerve Growth Factor
D – Day
BIIItub – Tubulin beta-3 chain

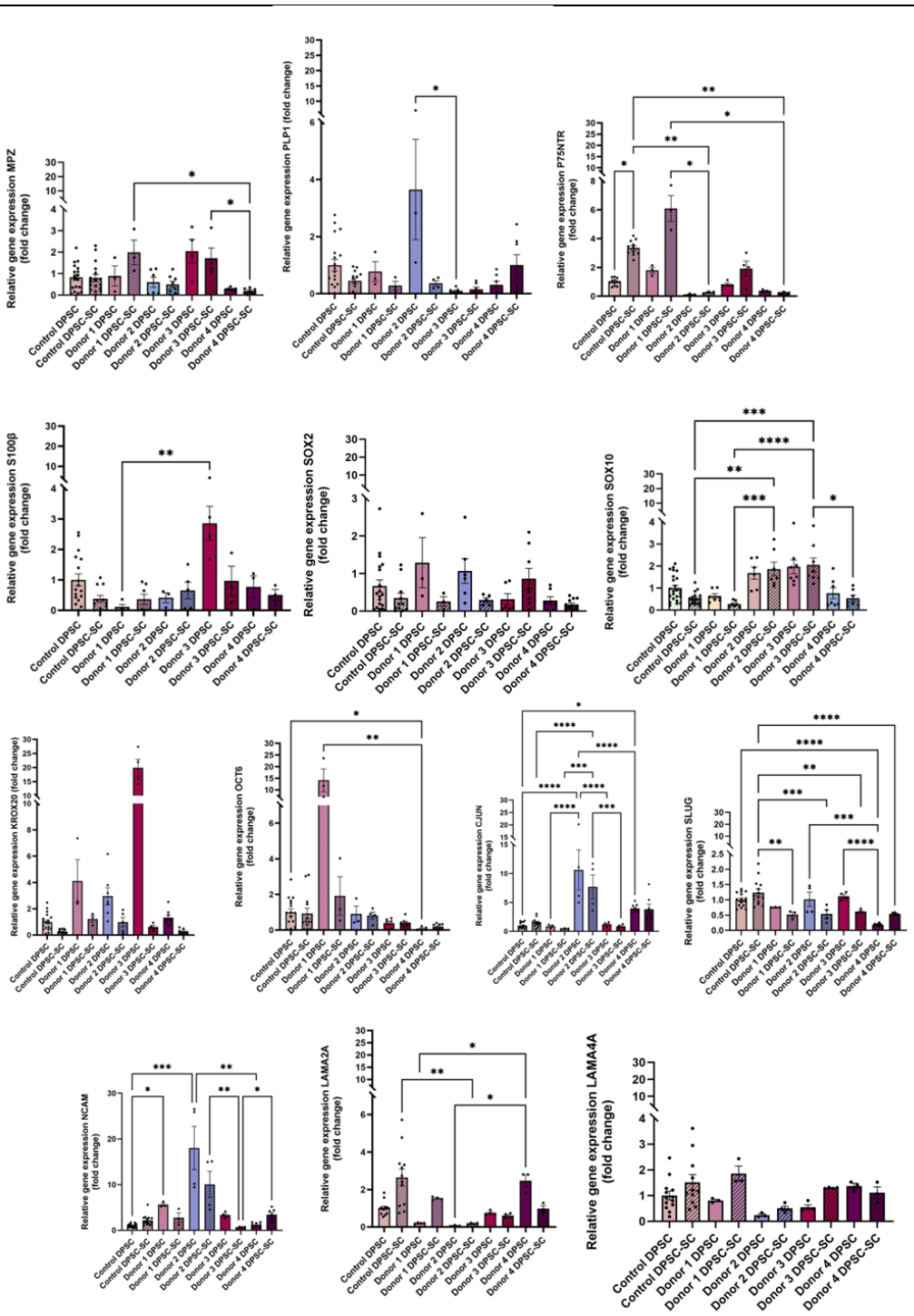

Supplementary figure 6 – mRNA expression levels of 13 SC-related genes: MPZ, PLP1, P75^{NTR}, S100β, SOX2, SOX10, KROX20, OCT6, CJUN, SLUG, NCAM, LAMA2A, and LAMA4A in four CMT1A-derived as well as a pool of control DPSC and DPSC-SCs. Data is presented as mean ± SEM, normalized toward the reference gene *PGK1* and the mean of control DPSCs per gene (N≥3). *P < 0.05, **P < 0.01, ***P < 0.001, ****P < 0,0001; (A-H; L-M) one-way Kruskal-Wallis test or (I-J) one-way Mann-Whitney U test followed by a Dunn's multiple comparison test. *Abbreviations are listed in Table S5.*